II. Distributed mass sensing experiments

The starting motivation behind the realization of distributed mass sensing experiments has been the development of a 'quasi-dynamic stencil' system (QDS) in partnership with EPFL. Such a system is supposed to achieve a relative motion between a full-wafer stencil and a substrate, so that multiple-layer nanostructures can be formed in-situ by shifting the stencil patterns in a step-and-repeat mode. In this way, high purity multi-material deposits can be structured and thereby very specific devices like tunnel junctions can be fabricated.

Within this context, the incorporation of a mass sensor below the stencil presents two interests. First, the material transport through confined geometries, i.e. nanostencil apertures, can be characterized in order to determine the local mass deposition rate on the substrate. Second, the sensor can be used for in-situ alignment of the stencil with respect to the substrate. The principle of operation is simple (see Figure 23): when the sensor is located below a dedicated stencil aperture, it detects a signal corresponding to a mass loading thus providing simultaneously the spatial position and the deposition rate:

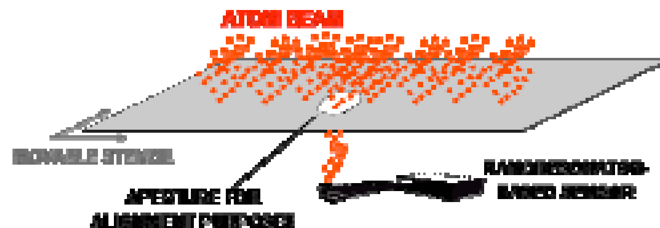

Figure 23. Schematic representation of a nanomechanical mass sensor implemented as position-sensitive sensor for nanostencil lithography systems

Resonating NEMS, like the previously presented ones, and quartz-crystal microbalances (QCM) are basically the two types of devices which are adequate for distributed mass sensing purposes (e.g. having the ability to detect the deposition of uniform thin layers). However, nano/micromechanical resonators should represent an important progress with respect to QCM as they feature a potentially higher mass sensitivity and an intrinsic higher spatial resolution due to their small size (in comparison, a QCM has a 1 cm^2 area).

Furthermore, QCM achieve their best performance when they are uniformly loaded over their entire surface. However in the QDS system, the beam is expected to have a diameter of few microns after passing through the apertures: in this case the QCM would be operated like in punctual mode (compared to its whole area). In these conditions, its performance is very poor as it has been demonstrated in Table VI - 1.

On the contrary, the nanomechanical resonator is operated in a distributed mass sensing configuration since the material beam is larger than it and uniformly coats it.

With the aim of implementing nano/microresonators as positioning sensors in the QDS system, their performance has been assessed in experiment III, whereby the in-situ monitoring of the deposition of ultra-thin gold layers has been realized. Meanwhile, a QCM, placed in the

vicinity of the NEMS has allowed (i) comparing NEMS and QCM performance and (ii) having a reference to estimate quantitatively the deposited mass.

For the purpose of the final application (in situ detection of ultra-thin layer deposition, in a high vacuum chamber), the target is the ability to measure a frequency shift corresponding to a 1 s shutter aperture time at a typical deposition rate of 0.3 nm/s for gold, silver and aluminum. The minimum detectable frequency shift is assumed to be around 100 Hz, what is voluntarily overestimated. First, the frequency shift as a function of the sensitivity is calculated in order to determine the NEMS mass sensitivity required in those conditions of operation. The deposited mass is given by:

$$\Delta \boldsymbol{m} = \rho \,\Delta \boldsymbol{e}\, \boldsymbol{A} = \boldsymbol{S_D}\, \Delta \boldsymbol{f}\, \boldsymbol{A} \qquad \text{(VI.15)}$$

where Δm is the mass of the on-top deposited layer, S_D the distributed mass sensitivity ($g{\cdot}cm^{-2}{\cdot}Hz^{-1}$), Δf the resulting frequency shift, A the resonator area, and ρ the density of the deposited material. Δe is the deposited thickness and can be expressed as:

$$\Delta \boldsymbol{e} = \frac{\boldsymbol{S_D}\, \Delta \boldsymbol{f}}{\rho} \qquad \text{(VI.16)}$$

Defining Δe as $\Delta \boldsymbol{e} = \boldsymbol{R}\, \boldsymbol{t}$ (R is the evaporation rate (nm/s) and t the evaporation time), one can also express the resulting frequency shift as:

$$\Delta \boldsymbol{f} = \frac{\rho\, \boldsymbol{R}\, \boldsymbol{t}}{\boldsymbol{S_D}} \qquad \text{(VI.17)}$$

In Table VI - 5, the frequency shift resulting from a 1 s deposition at a rate of 0.3 nm/s is reported as a function of the deposited material and of the distributed mass sensitivity:

Distributed mass sensitivity ($g{\cdot}cm^{-2}{\cdot}Hz^{-1}$)	1 10^{-9}	1 10^{-10}	1 10^{-11}
Δf (Hz) for Au deposition (ρ=19.3 $g.cm^{-3}$)	580	5800	58000
Δf (Hz) for Ag deposition (ρ=10.5 $g.cm^{-3}$)	320	3200	32000
Δf (Hz) for Al deposition (ρ=2.7 $g.cm^{-3}$)	80	800	8000

Table VI - 5. Frequency shifts associated to a given distributed mass sensitivity for a 1s deposition at a rate of 0.3 nm/s for gold, silver and aluminum

In order to exceed the frequency resolution of 100 Hz for any deposition material, an appropriate range for the distributed mass sensitivity is 10^{-10} - 10^{-11} $g.cm^{-2}.Hz^{-1}$, i.e. more sensitive than state of the art quartz microbalances ($1.23{\cdot}10^{-8}$ $g.cm^{-2}.Hz^{-1}$).

This section will be structured in the following way: first, the high performance in terms of distributed mass sensing of CMOS integrated nano/micromechanical structures will be demonstrated in experiment III. Second, the design of the QDS system will be described, focusing on the implementation of the mass sensor to achieve in-situ full-wafer alignment between stencil and substrate.

II.1. Monitoring the deposition of ultra-thin gold layers (exp. III)

This experiment has been carried out using a deposition chamber designed and assembled by Dr. Jordi Fraxedas from ICMAB-CSIC (Barcelona, Spain). Experiment III has consisted in placing inside the vacuum chamber a QCM and a CMOS chip containing integrated nanomechanical resonators (whose fabrication has been described in chapter 4) mounted on a PCB. Both have been simultaneously operated in order to monitor in-situ and in real time the deposition of ultra-thin gold layers (less than 0.1 nm thick).

Hereafter, the mains components of the experimental set-up are described, the choice and mode of operation of the nanomechanical sensor are discussed and finally an analysis of the main results is proposed.

II.1.a. Experimental set-up

DEPOSITION CHAMBER CHARACTERISTICS

The deposition chamber has been designed in order to be able to evaporate gold at low rates. In Figure 24, the vacuum chamber and its main components are depicted:

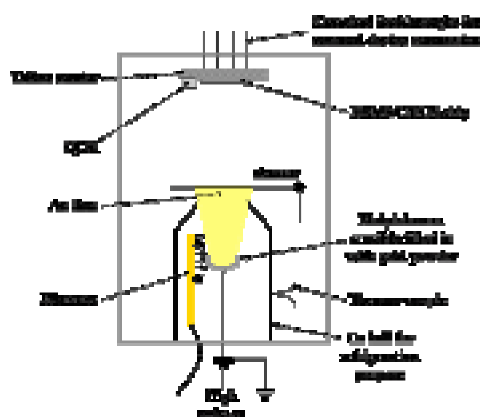

Figure 24. Scheme of the high vacuum evaporation chamber with its different components and the electrical feedthroughs. The configuration with closed shutter is depicted.

This is a hybrid deposition chamber: this is nor an electron beam neither a thermal evaporator but rather a combination of both. Under high vacuum conditions (around 10^{-7} mBar), a tungsten (W) filament is heated by a current flow so that it starts emitting electrons that impact on a closely located molybdenum crucible in which gold powder is stored. This crucible is polarized at a high voltage to attract the electrons and becomes heated by their bombardment. In this way, some Au is melt and evaporates isotropically. The surrounding bell is made of copper (Cu) and its temperature can be controlled by a thermo-couple. The Au beam can be confined to the bell by means of a shutter manually controllable from outside.

Operated at a pressure of 7 10^{-7} mBar, typical deposition parameters are a filament current of 1.83 A, an emission current of 25 mA (corresponding to the electron flux created by the filament, it flows into the crucible and the high voltage electrode), a flux current of 1.5 μA (corresponding

to ionized gold atoms, and measured by a probe in the vicinity of the crucible) and a polarization voltage of the crucible of 750 V.

The NEMS/CMOS chip is stuck on a PCB and wire bonded. This PCB is placed on a Teflon© carrier (see the white part in Figure 25) on which some metallic clips ensure both mechanical clamping and electrical contacts with the pads of the PCB. These clips are soldered in the lower side of the Teflon carrier to a series of wires connected to electrical feedthroughs that allow electrically connecting the device from outside the chamber:

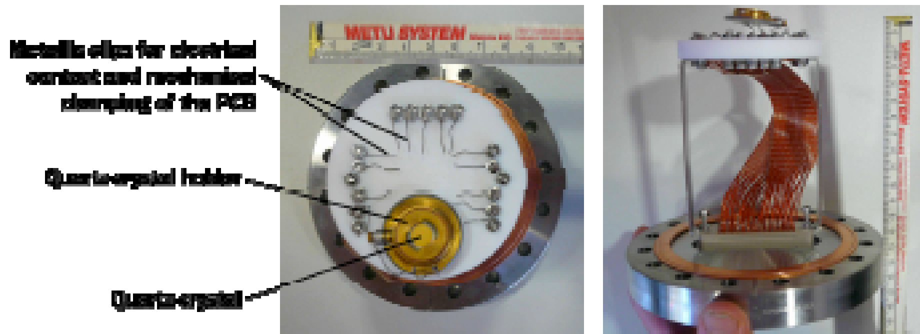

Figure 25. Pictures in top (left) and side (right) views of the sample holder (the PCB containing the chip is not present here)

OPERATION OF THE QUARTZ-CRYSTAL MICROBALANCE (QCM):

In the vicinity of the NEMS/CMOS chip, an AT-cut quartz-crystal (INFICON 008-010-G10, www.inficon.com) and its specific holder are placed just above the Teflon carrier so that the crystal is implemented as a microbalance. Actually, the holder is the genuine INFICON one but without the refrigeration network. Therefore the QCM cannot be controlled in temperature what can represent a major problem assuming that the quartz crystal temperature coefficient (in Hz/°C) is in the order of few ppm (part per million), in other words of few Hz (since its resonance frequency is the MHz range). The problem is that few Hz are precisely the expected range of frequency shifts caused by a mass loading of thin gold layers. The resonance frequency (around 6 MHz) is electrically measured in real time by a network analyzer (AGILENT E5100A).

To translate the resonance frequency shift related to mass loading into a value of deposited material thickness, mostly three methods exist: the 'Sauerbrey' [18] one, the 'period measurement' one and the 'Z-match' one [19]. These last two methods are more modern and are more accurate for already loaded quartz devices having experienced large frequency shifts. In our case, the 'Sauerbrey' [18] approach is followed since the devices are only used for ultra-small depositions (the maximum frequency shift to maintain the accuracy of the calculation is limited to 2% of the initial resonance frequency, here it would correspond to 120 kHz). This equation is only strictly applicable to uniform, rigid, thin-film deposits on the QCM active area that is restricted by the area of the rear contact electrode (0.6 mm in diameter). Assuming that this is the case, the deposited thickness Δe is given by [18]:

$$\Delta e = \frac{\rho_{QCM}\, e_{QCM}}{\rho_D\, f_I}\left(f_I - f_F\right) \tag{VI.18}$$

where ρ_{QCM} is the density of quartz crystals (about 2.65 g.cm^{-3}), e_{QCM} its thickness, ρ_D the density of the deposited material, and f_I and f_F the resonance frequency of the QCM before and after the deposition.

Assuming that the crystal vibrates longitudinally, the crystal thickness can be calculated by the following equation [20]:

$$e_{QCM} = \frac{N_{AT}}{f_I} \tag{VI.19}$$

where N_{AT} is equal to half the wavespeed for transverse waves: 1661 m.s^{-1} and f_I is the initial resonance frequency. For a 6 MHz QCM, eq.(VI.19) gives around 280 µm.

CHARACTERIZATION OF THE INTERNAL CONDITIONS OF THE DEPOSITION CHAMBER

The operation of the tungsten filament has likely an incidence on the internal temperature of the chamber what is problematic regarding the lack of temperature control for the QCM. In parallel, it emits radiations (in particular at X-ray, infra-red [IR] and visible wavelengths) which may perturb the CMOS circuitry.

The effect of the progressive aperture of the shutter until full illumination has been investigated placing in the vacuum chamber and very close a QCM and a temperature sensor (a wire bonded cross-bridge resistance (CBR) polysilicon structure).

This CBR has helped in assessing the internal temperature to know if during posterior mass experiments the QCM may exhibit frequency shifts related to temperature changes. A CBR structure (chip ref. 3157-13-6) made of n-type *poly1* (see chapter 4) has been wire bonded to the pads indicated in Figure 26:

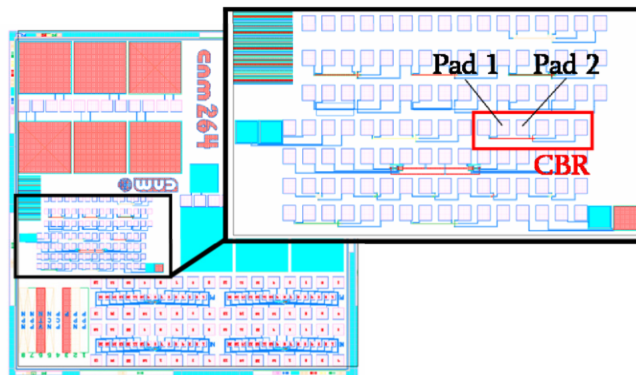

Figure 26. Position of the *poly1* CBR inside the chip, indicating the two bonded pads

The CBR is a simple polysilicon structure acting as a resistor of known dimensions that can serve to calculate the polysilicon resistivity. The sample has first been placed into an oven with controllable temperature. Sweeping from 25 °C to 80 °C, the temperature dependence has been measured: it exhibits a law of the type $R_T = R_0(1+\alpha T)$ where T is the temperature (in °C), R the resistance from pad 1 to pad 2 (in Ω) and α the temperature coefficient: R_0=1734 Ω and α= 0.7 10^{-3} /°C are deduced.

Then, the CBR has been placed in the vacuum chamber and the internal temperature has been monitored switching on the filament but without evaporating and progressively opening the shutter in four intermediate grades. The entire timeframe here is around two and a half hours.

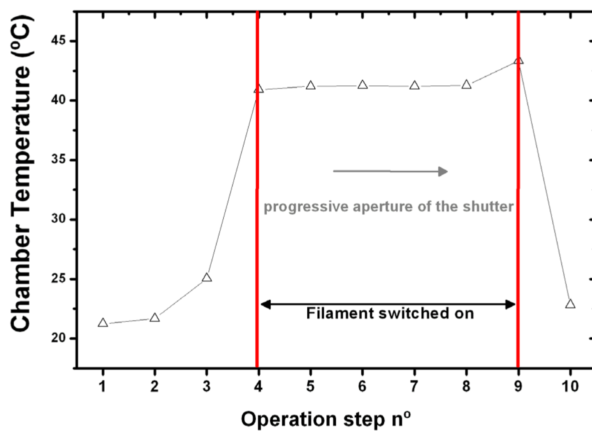

Figure 27. Internal temperature of the chamber as a function of the filament state and the grade of shutter aperture

Operation steps:

1: ambient conditions
2: in vacuum
3: in vacuum, one day later
4: filament switched on (t=0)
5: aperture grade 1 (t=1 min)
6: aperture grade 2 (t=1h02 min)
7: aperture grade 3 (t=1h12 min)
8: aperture grade 4 (t=1h18 min)
9: shutter completely opened (t=1h44 min)
10: shutter closed (t=2h30 min)

More than the grade of aperture itself, it seems that mostly the state of the filament (switched off or on) determines the internal temperature. It reaches 43.3°C after twenty minutes (maybe it would have increased even more after a longer time), i.e. more than twenty degrees above the room temperature.

Simultaneously, both a CCII circuit and a QCM have been monitored. Within one hour, the resonance frequency of the QCM increased of 2.8 Hz with the switched off filament. Then it was switched on and the resonance frequency evolution (normalized to 5.963544 MHz) has been recorded: it is reported in Figure 28 as function of the grade of shutter aperture:

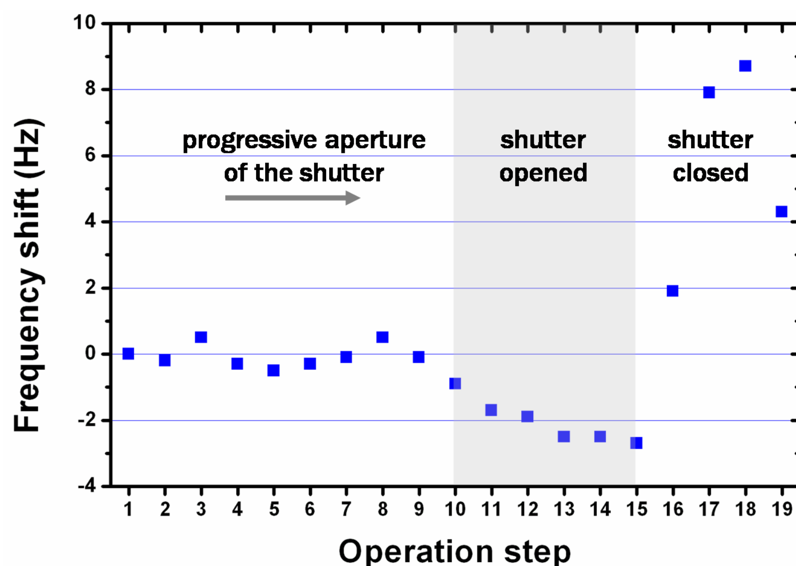

Figure 28. Variation of the QCM resonance frequency as a function of the aperture of the shutter and constantly switched on filament

Operation steps:
1: initial (t=0)
2: aperture grade 1 (t=1 min)
3: aperture grade 1 (t=13 min)
4: aperture grade 1 (t=59 min)
5: aperture grade 2 (t=1h04 min)
6: aperture grade 2 (t=1h08 min)
7: aperture grade 3 (t=1h15 min)
8: aperture grade 4 (t=1h20 min)
9: aperture grade 4 (t=1h41 min)
10: shutter opened (t=1h46 min)
11: shutter opened (t=1h53 min)
12: shutter opened (t=1h55 min)
13: shutter opened (t=1h59 min)
14: shutter opened (t=2h07 min)
15: shutter opened (t=2h13 min)
16: shutter closed (t=2h30 min)
17: shutter closed (t=2h45 min)
18: shutter closed (t=2h50 min)
19: shutter closed (t=4h28 min)

It seems that when the filament is switched on, the frequency fluctuates around a constant value independently of the grade of shutter aperture. When it is completely opened, the resonance frequency starts falling down slowly (about -2.5 Hz in 30 minutes) while the internal temperature increases of 2°C (see Figure 27). Recapitulating previous data, it can be stated that:

- the temperature increases of about 20 °C when switching on the filament
- when switching on the filament, we have observed a decrease of about 18 Hz in the QCM resonance frequency

As a conclusion, it seems that an increasing internal temperature makes decrease the QCM resonance frequency of about 1 Hz per Kelvin. Concerning the CMOS circuitry, its performance degrades drastically and rapidly when the shutter is totally opened, supposedly because of X-ray and IR radiations.

However, these results have to be considered with caution as in these proofs the relative orientation between the circuitry and the QCM with respect to the shutter has not been checked. In this context, one element may have been exposed before or after the other to the filament radiation. The CCII is maybe degraded even before a total exposure to the filament.

II.1.b. Nanomechanical sensor

The nano/micromechanical resonators used in experiment III are CMOS integrated in-plane vibrating cantilevers like the ones characterized in chapter 5. They have been defined by nanostencil lithography.

For measurements in vacuum, the associated high Q factor makes attractive CMOS integrated cantilevers compared to QB for three reasons. (i) thanks to the high Q, low driving voltages are enough to offer good electrical performance (in terms of magnitude and phase changes) (ii) Technologically speaking, CMOS cantilevers require less process steps as no protective SU8 layer needs to be coated and patterned. (iii) Regarding the distributed mass sensitivity, cantilevers and QB (with dimensions like the ones presented in chapter 5) have similar characteristics in the range of 10^{-10} $g.cm^{-2}.Hz^{-1}$ (see also chap.2, Figure 18), what is better than state-of-the-art QCM (typically 10^{-8} $g.cm^{-2}.Hz^{-1}$). The distributed mass sensitivity of in-plane vibrating cantilevers is:

$$\boldsymbol{S_D} = \frac{4\pi}{1.015}\frac{\rho^{3/2}}{\boldsymbol{E}^{1/2}}\frac{\boldsymbol{h}\boldsymbol{l}^2}{\boldsymbol{b}} \tag{VI.20}$$

where *l*, *b* and *h* are its length, width and thickness respectively

These CMOS cantilevers have been wire bonded to a PCB fixed to the Teflon holder by means of metallic clips which assume two functions. They mechanically clamp the PCB to the holder by leaning on the contact pads of the PCB (connected to the bonded wires): in this way they also electrically contact the resonator. This pre-existing solution is actually not optimal and should be improved in the future since the electrical contact is not very good. Measurements done with this set-up have generally been noisier than with measurement set-up nº 1 or 2 (see chapter

5). Moreover, the manual manipulation of the clips to place the PCB under them has several times induced electrostatic discharges which have stuck the cantilever to its in-front electrode.

II.1.c. Results and analysis

In the following experiments of gold deposition, the relative orientation of the QCM and the NEMS/CMOS chip has been carefully adjusted to ensure that both devices are equally exposed to the crucible so that they undergo the same temperature and radiation effect as well as they receive the same quantity of mass.

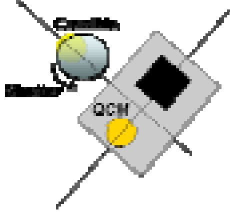

Figure 29. Top view of the orientation of the devices with respect to the atom beam

Initial tests have shown that the shutter can be only partially opened otherwise the signal of the NEMS/CMOS chip degrades rapidly until complete extinction. With regard to this matter, it has been observed that the deposition rate depends upon each grade of aperture. Furthermore this grade is not very precise as it relies on visual marks and the shutter screw was rather loose.

The measurement set-up is similar to the set-up nº2 described in chapter 5 except that the AC output of the network analyzer is commonly connected both to NEMS and QCM input ports while two separate input ports are used to get the output signals (the NEMS one with an input impedance of 1 MΩ, the QCM one with 50 Ω).

Two wire bonded CMOS cantilevers, very similar, have been used in the following experiments. Their characteristics are reported in Table VI - 6: geometrical dimensions, theoretical resonance frequencies $f_{0\ TH}$ and theoretical distributed mass sensitivity $S_{D\ TH}$.

device	l (µm)	b (nm)	h (nm)	$f_{0\ TH}$ (MHz)	$S_{D\ TH}$ (g.cm^{-2}.Hz^{-1})
WB-A	14.4	0.5	0.58	2.91	9.0 10^{-11}
WB-D	14.6	0.5	0.58	2.83	9.3 10^{-11}

Table VI - 6. Samples characteristics

Three sets of experiments performing several depositions have been carried out: two sets (nº1 and 2) with WB-D and one (nº3) with WB-A. The frequency shifts related to mass loading are monitored through the phase peak.

The QCM and the cantilevers have been excited with $V_{IN\ AC}$= 32 mV. The parameters of the CCII circuit are R_{LOAD}≈800 Ω and R_{POL}≈180 kΩ. In the first and second set with WB-D, $V_{IN\ DC}$ is set to 8 and 8.4 V respectively, and in the third with WB-A to 8.5 V.

To simultaneously monitor the deposition of gold atoms onto the resonator surface and onto the quartz surface, three approaches have been followed.

Being the objective the demonstration of the NEMS high mass sensitivity and taking into account that the low deposition rate of the evaporator is reduced by only partially opening the shutter, ultra-small deposits have successfully been formed but they have been impossible to

image neither with AFM nor with SEM. Furthermore, the circuitry could not be exposed a long time to the atoms beam owing to its sensitivity to the radiations emitted by the filament.

In practice, within the permitted short timeframe (because of the circuit sensitivity to the radiation), we have been able to observe frequency shifts of the cantilever in the order of hundreds of Hz.

As aforementioned, these CMOS cantilevers are nominally around 100 times more sensitive than QCM. As a result, the QCM has always been operated in its detection limit if one considers that the expected resulting shifts were in the order of few Hz and the opening/closure of the shutter has typically brought about few Hz shifts because of the lack of temperature control. Consequently, in all the results presented hereafter, the QCM shifts have been difficult to separate between temperature- and mass loading related shifts.

A first approach, that constitutes a proof of the successful operation of the resonator as mass sensor, has consisted in recording in real time the cantilever resonance spectra during the deposition, while the QCM was measured just before and just after this deposition.

This means that the quartz crystal does not experience any vibration while the cantilever is permanently excited during the evaporation and constantly vibrates in the plane. With regard to this matter, it is assumed that this motion, in the order of 1-10 nm according to chapter 5, Table V.7 and V.8, does not perturb the binding of atoms onto the surface and that it collects the same amount of mass as if it were static. In Figure 30, resonance spectra are recorded before, during and after a 3 minutes long deposition. In this example, the resonance frequency showed a good stability within a timeframe of 10 minutes after the end of the deposition.

This stability combined to the fact that the frequency shifted down to lower frequencies in a relatively linear dependence upon the deposition time indicate that these shifts are surely caused by mass loading. The total frequency shift is of minus 745 Hz approximately.

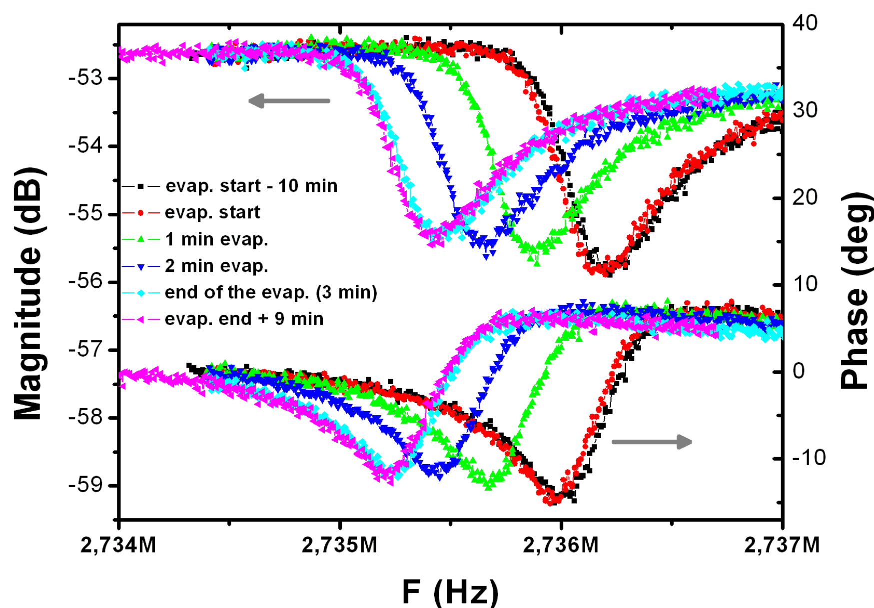

Figure 30. Set 1, WB-D device. Constant monitoring of the cantilever resonance signal during a 3 minutes long gold deposition by evaporation (span around 3 kHz)

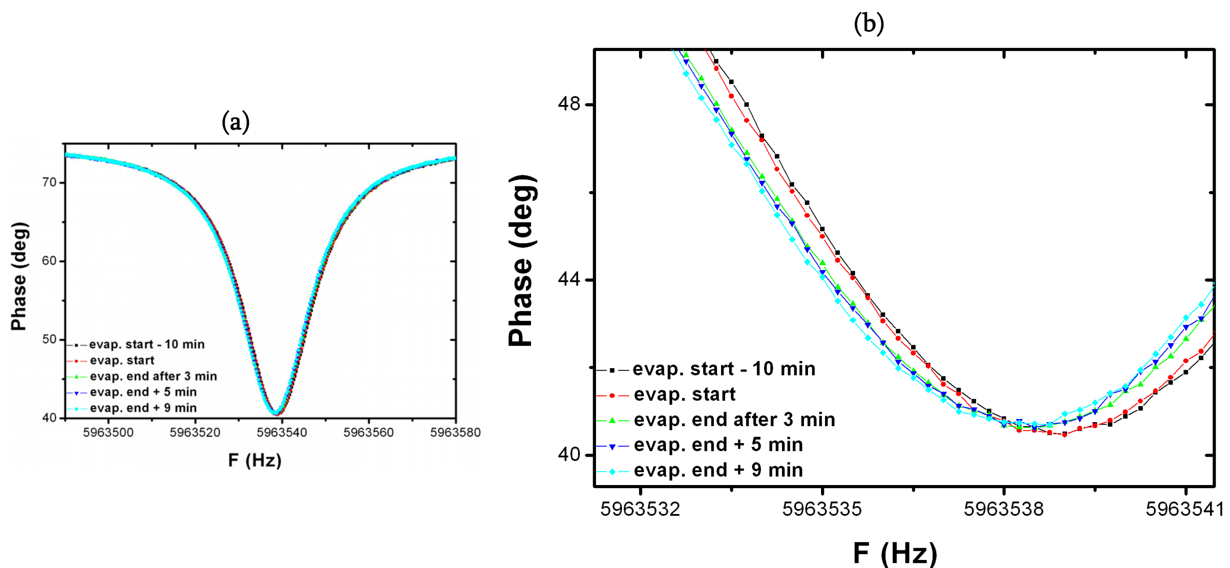

Figure 31. QCM resonance spectra (phase) measured before and after a 3 minutes long gold deposition by evaporation. In (a) span of 90 Hz, in (b) span of about 10 Hz [zoom of (a)]

In Figure 31(a), the resonance spectra of the QCM before and after the 3 minutes long deposition are reported inside a span of 90 Hz (the Q-factor is much higher). However, the corresponding shifts are so small that a zoom depicted in Figure 31(b) is needed to visualize any change. Before and after the deposition, the QCM resonance frequency seems relatively stable. The deposition resulted in a frequency shift of approximately minus 0.5/0.75 Hz, i.e. three orders of magnitude less than the cantilever.

Complementarily with the first one, the second approach has consisted in recording in real time the QCM resonance spectra during the deposition, while the cantilever was measured just before and after this deposition.

This means that the quartz crystal is permanently excited during the evaporation. In Figure 32, resonance spectra of the QCM are again recorded inside a span of 90 Hz for a 3 minutes long evaporation while in Figure 33 the cantilever resonance spectra are recorded before and after the deposition.

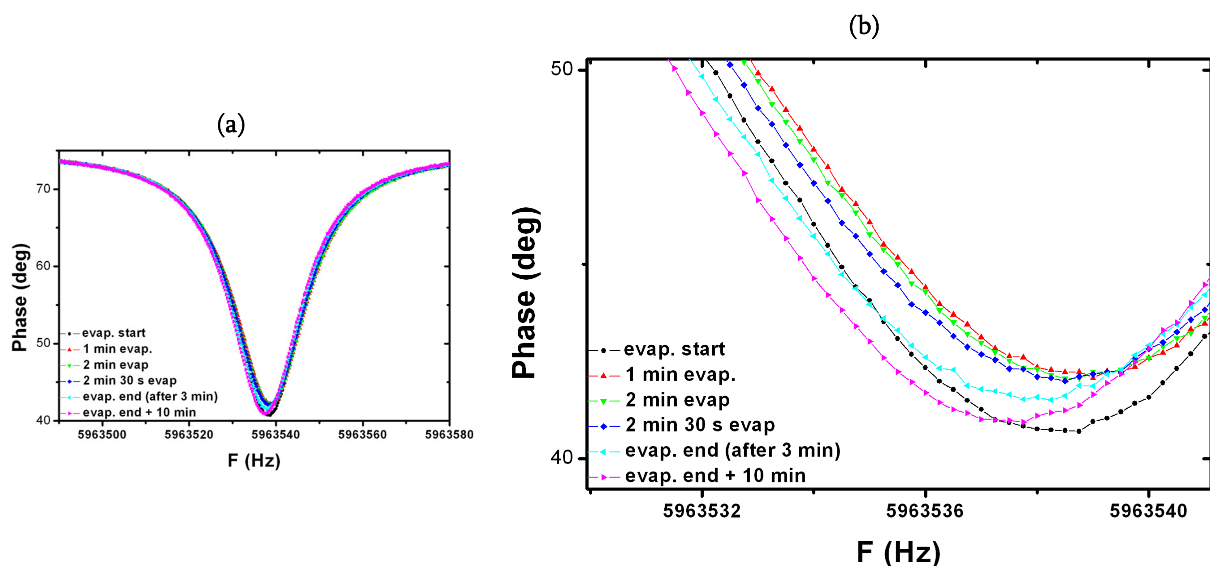

Figure 32. Constant monitoring of the QCM resonance spectrum (phase) during a 3 minutes long evaporation with a span of (a) 90 Hz, (b) about 10 Hz [zoom of (a)]

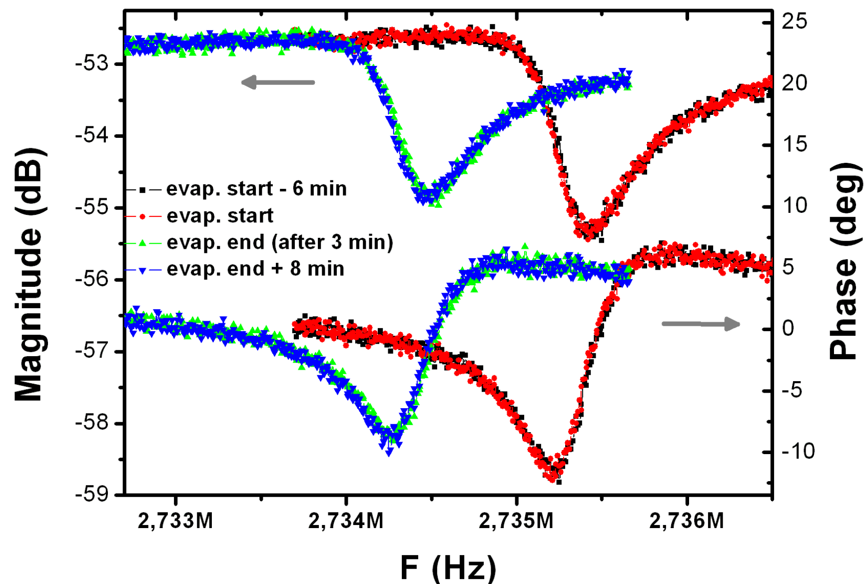

Figure 33. Set 1, WB-D device. Cantilever resonance spectra measured before and after a 3 minutes long evaporation with a span of about 3500 Hz

In Figure 32(a), the 90 Hz span has again been too large for the resulting small frequency shifts. A zoom is depicted in Figure 32(b) where a more complex pattern appears compared to Figure 31(b). Between the black curve (deposition start) and the red one (after 1 minute of deposition), the resonance shifts upwards and then decreases in posterior curves. This matter is not coherent with the observed negative shift of Figure 28 when opening the shutter. This indicates that without temperature control, a QCM operated in its resolution limit is not reliable enough to assess the deposited thickness.

However to try to extract any quantitative information, which shift could be considered? Between the black and the light blue curves (deposition start and end) of Figure 32(b), there is approximately a minus 0.5/0.75 Hz deviation. But if one considers the difference between the red and the light blue curves (respectively after 1 and 3 minutes of deposition), a larger deviation is observed (approximately minus 1.25 Hz). This value is maybe underestimated since in the first minute of evaporation, no spectrum has been recorded and the positive shift may still have been larger. In comparison, the cantilever resonance shift is much more significant as it exhibits a total deviation of minus 920 Hz.

The third approach has consisted in monitoring at a fixed frequency $f_{SPAN\ 0}$ the evolution of the cantilever signal during the deposition.

In this case, a resonance spectrum has to be recorded before the deposition (red curve in Figure 34) in order to determine the value of frequency where the phase peak is at its steepest transition. Then, the phase is scanned at this fixed frequency (by setting the span to 0). In the example of Figure 34, the grey straight line indicates that the oscillations of the cantilever are set to 2.92462 MHz.

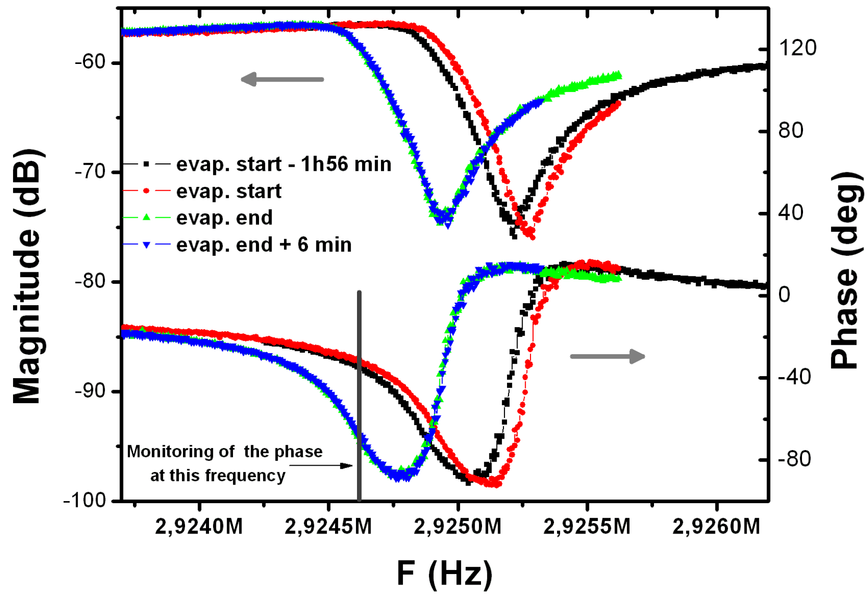

Figure 34. Set 3, WB-A device. Cantilever resonance spectra measured before and after several depositions (2 min 40 s in total) with a span of about 2500 Hz

While continuously monitoring the cantilever signal at the fixed frequency (here $f_{SPAN\ 0}$), four sequential evaporations of 40 seconds each have been performed. The resulting evolution of the phase signal is depicted in Figure 35(a): the grey bars indicate when the shutter is partially opened, i.e. when some gold is deposited. The final phase level is about 70°, what is confirmed by the spectra recorded just after the end of the depositions: see blue and green curves in Figure 34.

With a mathematical treatment, it is possible to convert the phase evolution of Figure 35(a) into a real-time evolution of the resonance frequency. Although the phase peak is not symmetrical, its left part (expressed as φ) can be fitted very accurately by a Lorentz function $L(f_{RES})$ centered on the phase peak (considered as the resonance frequency f_{RES}):

$$\varphi = L\left(f_{RES}\right) = \varphi_0 + \frac{2a}{\pi}\frac{b}{4\left(f - f_{RES}\right)^2 + b^2} \qquad \text{(VI.21)}$$

where a and b, and φ_0 are fitting parameters related to the curve width and to the phase offset respectively. Assuming that the initial and the final phase spectra conserve the same characteristics (offset and width), the left part of the curve is fitted so that a, b and φ_0 are determined. Then, setting the frequency at $f_{SPAN\ 0}$, f_{RES} can be obtained from φ applying the inverse function $f_{RES} = L^{-1}\left(\varphi\right)$:

$$f_{RES} = L^{-1}\left(\varphi\right) = f_{SPAN\,0} \pm \frac{1}{2}\sqrt{\frac{2ab}{\pi\left(\varphi - \varphi_0\right)} - b^2} \qquad \text{(VI.22)}$$

In this specific case, the sign is (+) since $f_{SPAN\ 0}$ is always inferior to f_{RES}.(see Figure 34). In this way, the curve of Figure 35(b) is obtained:

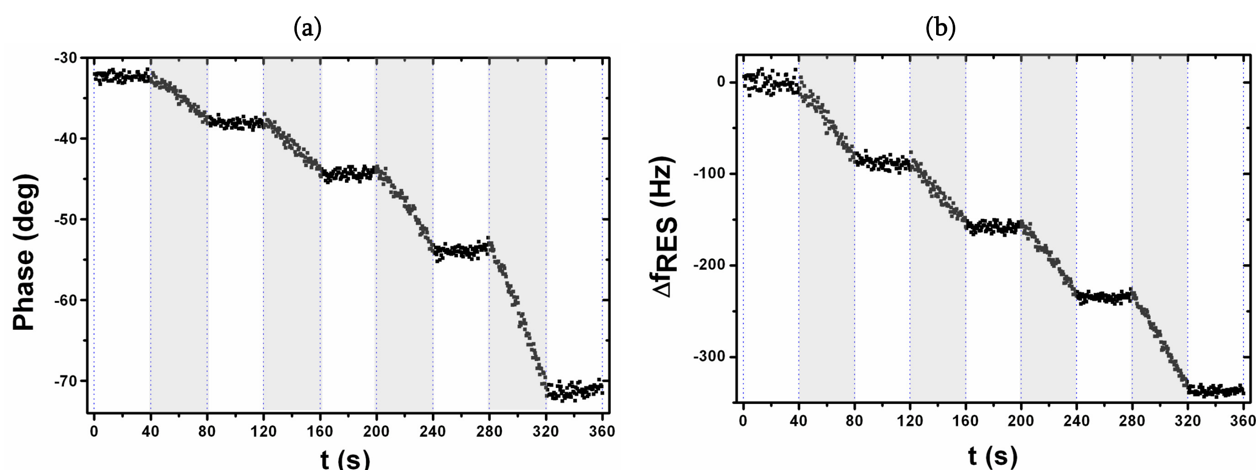

Figure 35. (a) Monitoring of the phase evolution in a 6 minutes time span during which 4 depositions of 40 s each are performed (illustrated by the grey bars). (b) Corresponding curve of resonance frequency shift evolution obtained by the transformation of the phase curve applying the inverse Lorentz function

This curve of Figure 35(b) coherently features (i) flat plateaus when the shutter is closed and (ii) linear shifts towards lower frequencies when the shutter is partially opened. The differences of slope between the successive evaporations are likely related to different deposition rates because the shutter has not been opened each time exactly in the same way, rather than to artifact of the mathematical method.

The example of Figure 35(b) shows that the presented mathematical strategy is effective, provided the phase signal presents significant derivatives. It is a straightforward and convenient method to track the evolution of the resonance frequency just by measuring the phase.

STABILITY AND NOISE CONSIDERATIONS

Both the QCM and the cantilever have exhibited a drift of resonance frequency when the filament was switched on. Over large timeframes, the cantilever seems to stabilize and the drift is much attenuated. This means that during a gold deposition of few minutes the contribution of the thermal drift to the resulting frequency shift can be neglected.

To estimate the noise featured by the CMOS cantilever, the cantilever phase signal has been recorded at a fixed frequency where the phase presents a steep evolution (like where the grey line is located in the blue curve of Figure 34). Figure 36 plots the phase signal as function of the time. The signal shows a drift of about 5.5° over 10 min and exhibits a permanent fluctuation.

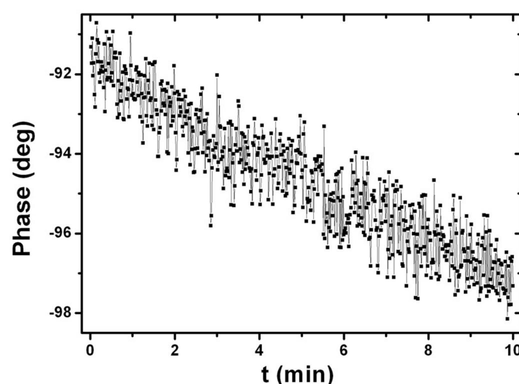

Figure 36. Phase noise measured during 10 minutes at a fixed frequency of 2.926286 MHz (in the pre-recorded spectrum, it is where the steepest point of the phase signal is located)

The phase noise is in the order of 2° peak to peak, i.e. 1.4° RMS. Taking into account the local slope of the variation of phase versus frequency, the resulting frequency noise has been estimated around 8 Hz RMS. (in chapter 5, we analyzed the different sources of noise that affect the output signal of the NEMS/CMOS system and the CMOS circuit was found to be the dominant source).

This value of frequency noise Δf_{NOISE} directly determines the minimum detectable mass Δm_{MIN} through the relation:

$$\Delta m_{MIN} = S \, \Delta f_{NOISE} \tag{VI.23}$$

where S is the mass sensitivity (in g.Hz^{-1})

SUMMARY OF THE RESULTS

In the three sets of experiments, multiple depositions have been carried out. In Figure 37, Figure 38 and Figure 39, the resonance frequency shifts of QCM and cantilevers are plotted as a function of the deposition steps.

In Figure 37, the QCM exhibits at the beginning a large negative shift although no gold seems to have been deposited until gold evaporation nº5 if one relies on the cantilever behavior (previous 'evaporations' were operation tests only to calibrate the shutter aperture). This peak must be likely neglected as the large timeframe indicates a long stabilization time because of thermal drift. Afterwards, both curves do no follow perfectly parallel evolutions but in order to try to extract any quantitative information, the shifts resulting of evaporations 5 to 9 are considered and reported in Table VI - 7. The same in Figure 38, only the shifts resulting of evaporations 11 to 13 are considered, and in Figure 39 the shifts of evaporations 5 to 8.

From the QCM resonance frequency shift, an equivalent thickness Δe is calculated with eq.(VI.18). Using this value and the measured frequency shift of the cantilever Δf_{RES}, the experimental distributed mass sensitivity $S_{D\ EXP}$ can be obtained in this way (see eq.(VI.15)):

$$S_{D\ EXP} = \frac{\rho_{Au} \, \Delta e}{\Delta f_{RES}} \tag{VI.24}$$

All the results are reported in next table. It also provides the values of deposited thickness theoretically calculated using the mass sensitivities of Table VI - 6 and eq.(VI.16):

Set	Device	Δf_{RES} QCM (Hz)	Δe (nm)	Δf_{RES} Cant. (Hz)	Δe_{TH} (nm)	$S_{D\ EXP}$ (g.cm^{-2}.s^{-1})
1	WB-D	2.5	0.016	2550	0.123	1.2 10^{-11}
2	WB-D	3.25	0.021	1220	0.059	3.3 10^{-11}
3	WB-A	2.5	0.016	2000	0.093	1.5 10^{-11}

Table VI - 7. Experimental results of the three sets of experiments and resulting experimental distributed mass sensitivity

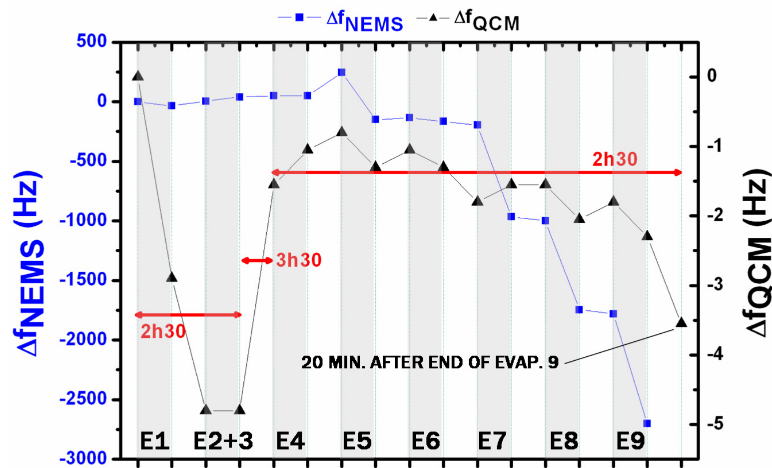

Figure 37. Set 1, WB-D. Resonance frequency shifts of cantilever and QCM as a function of successive depositions of gold by evaporation (represented by a grey bar and named E#)

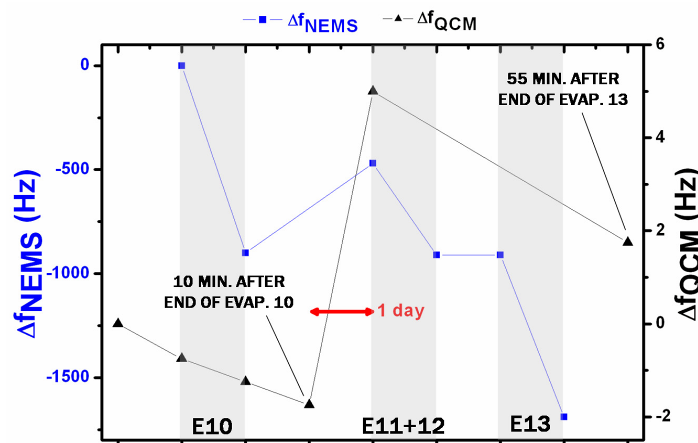

Figure 38. Set 2, WB-D. Resonance frequency shifts of cantilever and QCM as a function of successive depositions of gold by evaporation (represented by a grey bar and named E#)

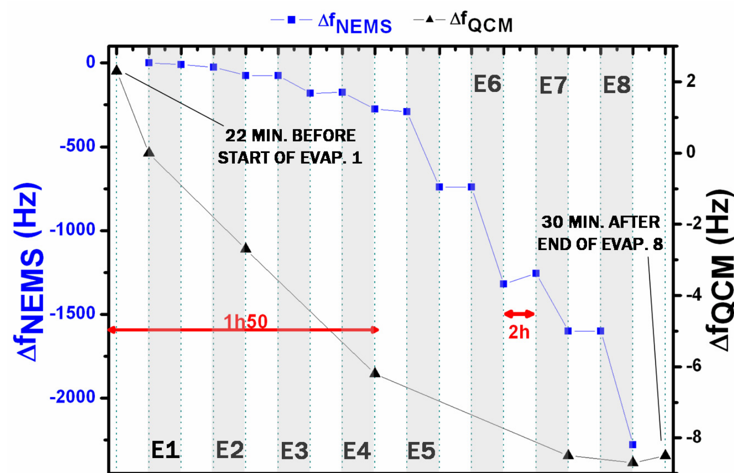

Figure 39. Set 3, WB-A. Resonance frequency shifts of cantilever and QCM as a function of successive depositions of gold by evaporation (represented by a grey bar and named E#)

The apparent total thickness deposited during each set is inferior to the tenth of nanometer (0.1 nm), what indicates that not even a monolayer has been formed on the cantilever surface after each set. Probably, the deposits are under the form of localized clusters which remain too small to be imaged. This would have helped in having another reference than the QCM which did not provide reliable quantitative information on the amount of deposited mass. Indeed, the QCM has been operated without temperature control and in its detection limit. For example, there is no reason to find a difference of mass sensitivity by a factor 3 between sets 1 and 2 although both sets were realized with the same cantilever. Apart from the uncertainty in the QCM shift, other sources of error arise from data not provided by the QCM fabricant like its precise thickness and active area, which have been roughly estimated.

The apparent distributed mass sensitivity of the cantilevers is between 2.8 and 7.8 times better than the theoretical value (see Table VI - 6). In this sense, experiment III qualitatively confirms the high mass sensitivity of cantilever resonators. The theoretical calculation of sensitivity seems to provide the correct order of magnitude (but from those results it cannot be concluded if accurately or not). Furthermore, curves like the one of Figure 35(b) confirm the linearity of the mass sensor (this type of curve has been repeated several times).

ADDITIONAL REMARKS

A first remark concerns the specific behavior of CMOS cantilevers within this set-up. From Figure 30 and Figure 33, it is clear that both magnitude and phase degrade along the depositions. Observing that it did not occur in experiments I and II, we make the assumption that this progressive decrease is not related to a mass loading but to the successive irradiations which degrade the CMOS circuitry according to complex physical processes. In this sense, experiment IV is going to provide additional information on this topic assuming that the circuitry will not be exposed to any irradiation as it will be covered by a nanostencil membrane.

The second remark concerns the validity of attributing the entire frequency shift to mass loading. When some material is adsorbed on a nano/micromechanical resonator, the produced shift is the combination of three contributions: one related to adsorption-induced surface stress [12, 21], another to the adsorbate stiffness that modify the effective Young modulus [11], and the third related to the proper mass loading. The two first contribute to shift the resonance upwards while the third downwards. It has been reported [22, 23] that metal deposits under the form of a single monolayer can result in a dominant stress effect and thereby in a shift upwards. In the example of experiment III, the gold thickness is so thin that the negative shift is probably entirely related to mass loading. However, a further study would be to perform theoretical calculations combining the three effects in order to predict the cantilever behavior for larger deposited thicknesses.

II.2. Application of NEMS/CMOS mass sensors as positioning sensors (exp. IV)

In experiment III, CMOS cantilevers have exhibited a linear behavior during mass depositions and have fulfilled the requirements in terms of distributed mass sensitivity listed in Table VI - 5. These specifications have been defined to further implement NEMS-based mass sensors as alignment sensors within a quasi-dynamic stencil lithography system (QSD). This system is presently being developed with EPFL. The first deposition experiments are scheduled for October 2007.

Hereafter, first progresses towards the realization of a demonstrator of the QDS concept are detailed: the QDS approach is introduced and the system is described focusing on the requirements that the alignment sensor has to fulfill.

II.2.a. Quasi-dynamic approach

The goal is to use full-wafer sized stencil and substrate in combination with a large range, highly accurate XY nanopositioning stage to perform stencil lithography in a quasi-dynamic approach. The patterning procedure consists in (i) aligning stencil and substrate within the vacuum chamber, (ii) putting them in contact, (iii) evaporating a material through the nanostencil apertures, (iv) stopping the deposition and separating them again, (v) performing a controlled motion, (vi) putting them in contact and evaporating again, eventually with another material.

Repeating n-times this step-an-repeat approach, multiple (n) nanometer-sized patterns of multiple (n) materials can potentially be obtained. A decisive advantage of this technique is the opportunity to form high purity deposits since the vacuum is not broken in-between each deposition step. In this way, specific devices like tunnel junctions can potentially be fabricated. Racz et al.[24] made a first attempt of realization of QDS but using a different approach.

Thus, a system for full-wafer (100 mm) evaporation needs to be developed. The idea is to externally roughly pre-align the stencil to the substrate, to place the holder containing the two pieces into an evaporation chamber and to perform inside a finer alignment relying on the mass sensor. Once both elements are correctly positioned one with respect to the other (a 2-3 μm accuracy is aimed), the evaporation step starts. In between each subsequent evaporation step, the stencil is translated by two independent nanopositioning stages which have a 25 mm range and an encoder resolution of 20 nm. In the first demonstrator, the necessary motion between each deposition step is realized relying on the high resolution of the stage what conveniently avoids any posterior alignment step with the mass sensor.

II.2.b. System description

The guidelines of the QDS system are presented hereafter. The development is still on going and is not complete. The idea is to maintain fixed substrate and mass sensor while the stencil is linked to the translation stages. Like in static Stencil Lithography (SL), the gap between stencil and substrate needs to be controlled during the deposition in order to improve the patterning resolution. The gap must also be controlled during the stencil motion because of wafer curvatures that may cause frictions. The first version of the system is sketched in Figure 40: the substrate is located above the stencil and below the mass sensor.

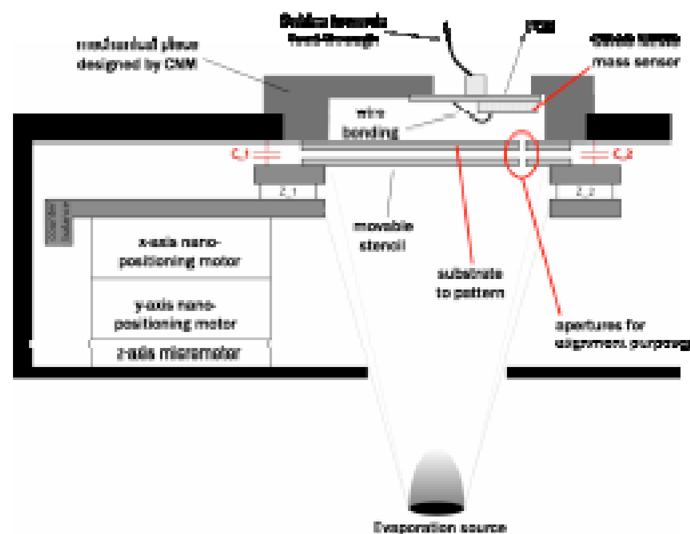

Figure 40. Schematic representation of the QDS system.

The gap between stencil and substrate is measured using three capacitive sensors (C_1, C_2 and, C_3 [not visible in the 2D scheme of Figure 40]) and controlled using three piezo-actuators (Z_1, Z_1 and, Z_3). During the phase of approximation of the stencil towards the substrate, the capacitive sensors indicate a progressively decreasing distance. When the measurement of distance becomes constant while the actuators are still pushing the stencil against the substrate, it means that both elements are effectively in contact (at least, in the three points of measurement).

This 'contact detection' can be performed over all three actuators in order to determine the correct position of the stencil with respect to the substrate. Actuation and sensor feedback signals have to be controlled by software. This software must simultaneously control and coordinate the following elements:

- XY actuation of the nanopositioning table
- active gap control. This consists in monitoring in real time the gap between substrate and stencil and therefore to actuate the stencil adequately through the three piezo. When touching, the procedure must be interrupted and the position must be memorized for further steps.
- stencil/substrate alignment procedure. A special scanning motion of the stencil must be carefully defined in order to provide a rapid and accurate alignment. The software must be connected to the network analyzer that measures in real time the frequency spectrum of the sensor. The phase change is monitored at a fixed frequency: the RMS value is continuously calculated and when it changes by twice the measured RMS noise, it means that the aperture is above the sensor and the position is memorized by the software.

The critical issue that determined the first guidelines of the system design has arisen from the need to be able to electrically connect the NEMS/CMOS chip. To simplify the packaging, a classical solution has been adopted based on bonding wires from the contact pads of the circuitry to a PCB. The height of these wires, given by their vertical curvature, implies an important gap in

the order of few mm between substrate and mass sensor. This has important consequences upon the sensor specifications.

The mechanical part on which the PCB is fixed has been already designed according to all these requirements: its schematic can be found in annex A.8. Another critical issue has arisen from the difficulty to find a straightforward and reliable method to fix substrate and stencil to their respective holder. This issue is circumvented through the use of stiff clips (see fig.4 in annex A.8).

II.2.b.i) Alignment procedure

The first operation consists in roughly pre-aligning the substrate above the mass sensor. In order to make it easier, a matrix of relatively large apertures (tenths of microns) is fabricated onto the substrate according to the standard microstencil fabrication process of EPFL. This operation is illustrated in Figure 41: the mass sensor is roughly positioned within one of those large apertures.

In order to obtain a spatial reference of the stencil aperture with respect to the substrate, our idea is to rely on the borders of one of the rectangular-shape apertures made in the substrate. Basically, when the stencil hole dedicated to alignment purposes is on top of the substrate, no flux passes [see Figure 41(a)], but whenever the hole arrives at one border, the mass sensor starts detecting it [see Figure 41(b)].

Figure 41 illustrates the alignment procedure in the X-direction (in the Y-direction the procedure is equivalent): the point here is that the flux is much enlarged when impacting on the surface because of the large gap between substrate and sensor. This feature is numerically described in next section [II.2.b.ii). Mass sensor requirements].

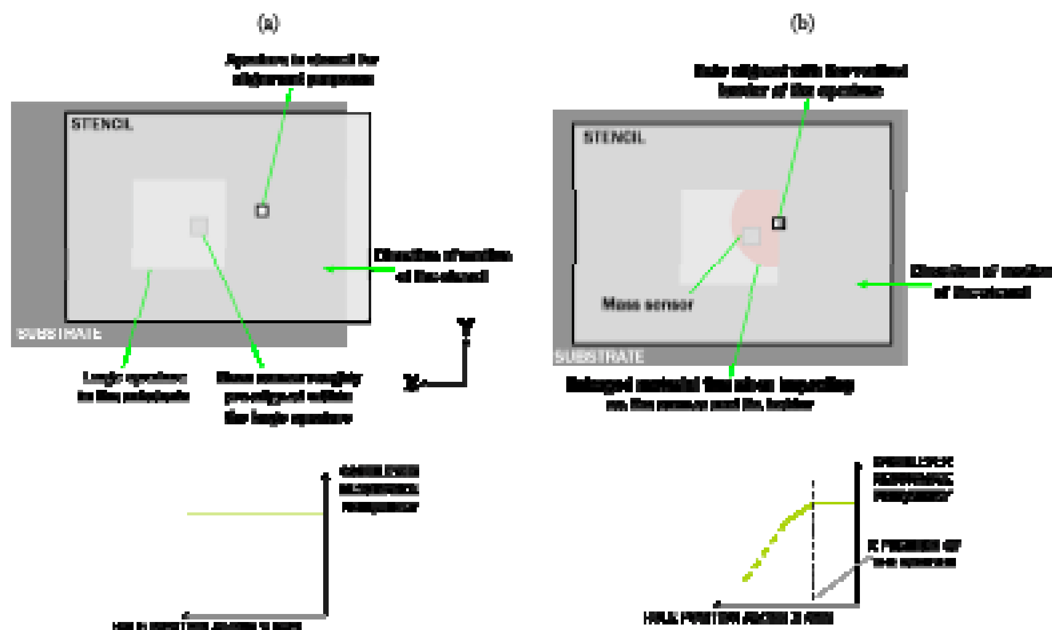

Figure 41. Alignment principle in the X direction. The stencil is schematically drawn transparent in order to make visible the underneath elements. (a) the stencil hole is above the substrate and no material impacts on the sensor. (b) the stencil hole arrives at the border of a substrate aperture and some material starts impacting on the cantilever sensor so that its resonance frequency starts decreasing

In fact, the precision of the system is determined by the ability to detect a fast and steep deviation of cantilever resonance frequency. The faster and the more pronounced is the transition between the plateau and the decreasing slope [see Figure 41(b)], the most precise is the determination of the X-axis spatial reference provided by the X-coordinate of the border. Actually, the faster and the more sensitive is the mass sensor, the most accurate will be the alignment.

To schematically illustrate alignment and deposition sequences, all the operation steps are sketched from Figure 42 to Figure 46:

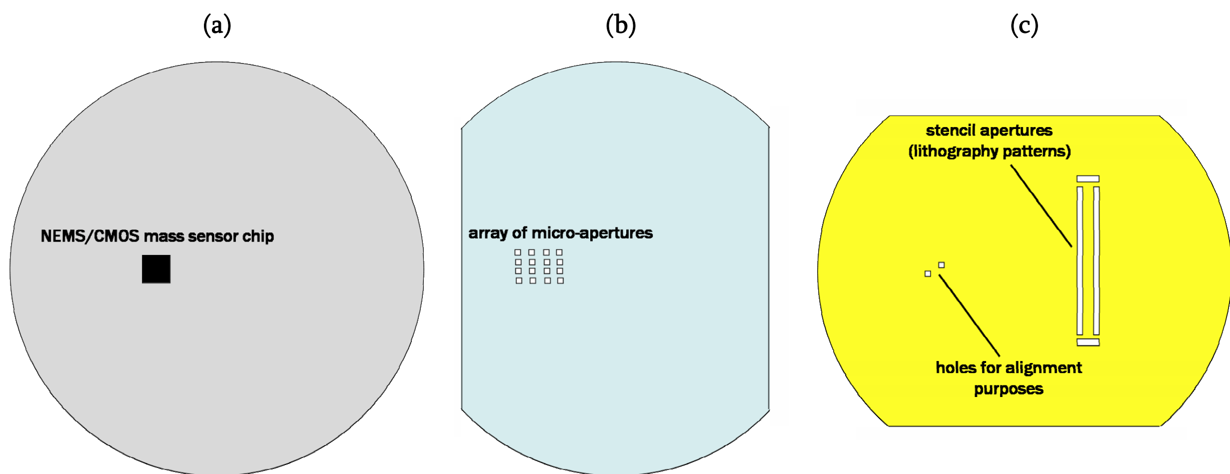

Figure 42. Schematic representation of the three elements involved in the alignment procedure. (a) NEMS/CMOS mass sensor chip. (b) substrate with an array of micro-apertures. (c) stencil containing holes for alignment purposes and other holes for patterning purposes.

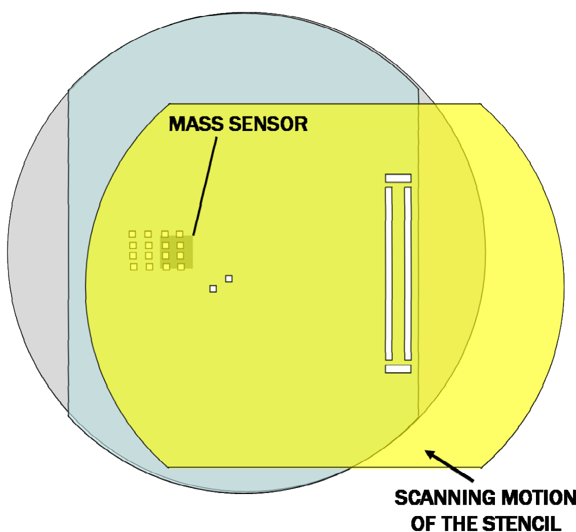

Figure 43.
STEP 1: substrate and sensor roughly pre-aligned externally. Start of the alignment procedure by moving the stencil while some material starts to be deposited

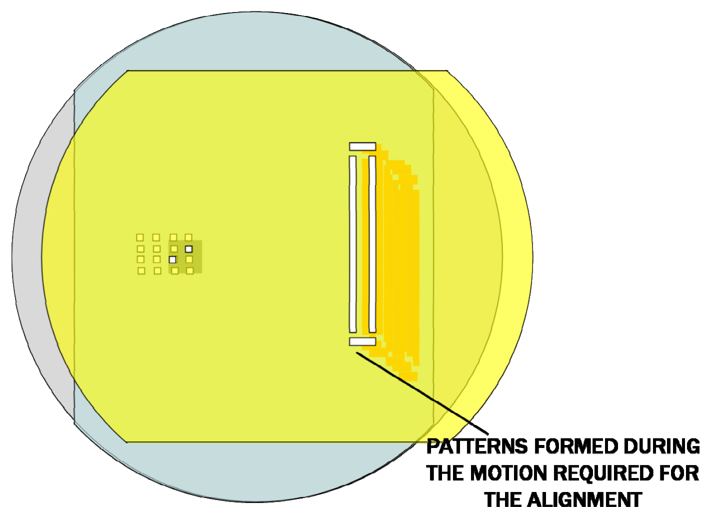

Figure 44.
STEP 2: stencil moved above the substrate. The scan lasts until a signal is detected by the mass sensor, corresponding to an alignment between stencil aperture and one of the substrate apertures. During this procedure, the substrate is already “drawn” due to the motion.

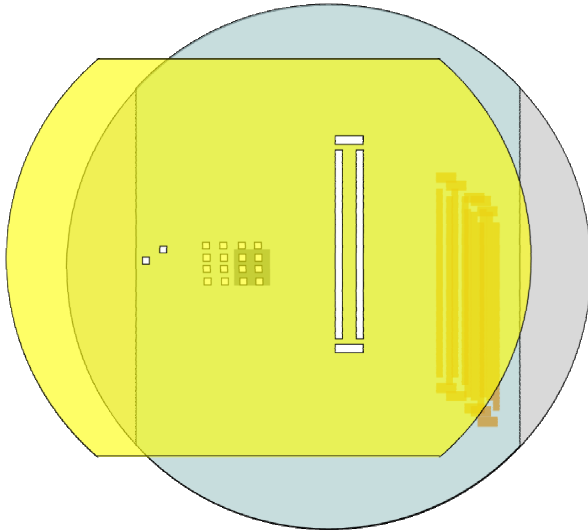

Figure 45.
STEP 3: Now the position is known, the deposition is stopped. The stencil is displaced until a given position.

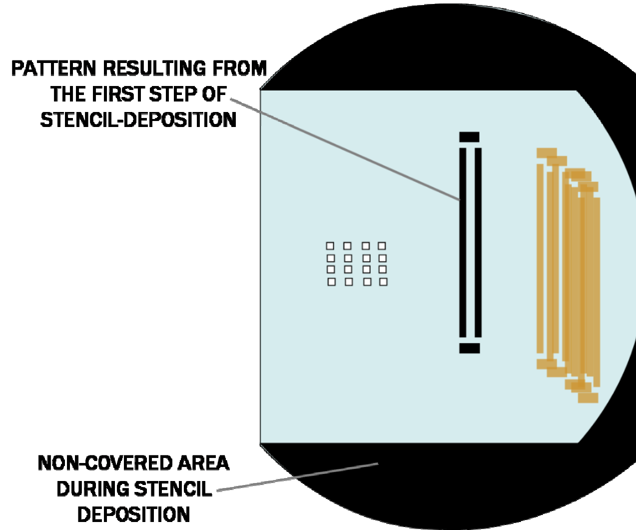

Figure 46.
STEP 4: Metal deposition. This scheme depicts the substrate after the alignment procedure and after a single metal deposition.

II.2.b.ii) Mass sensor requirements

Owing to the large gap between substrate and mass sensor (because of the height of the bonding wires), the atom flux is dispersed over a large area when impacting on the sensor chip. For this reason, the quantity of material potentially received by the mass sensor is much attenuated and will actually depend on the size of the stencil aperture. In the following section, these considerations are numerically assessed, in particular to estimate the time response of the sensor. Figure 47 sketches the critical dimensions of the system:

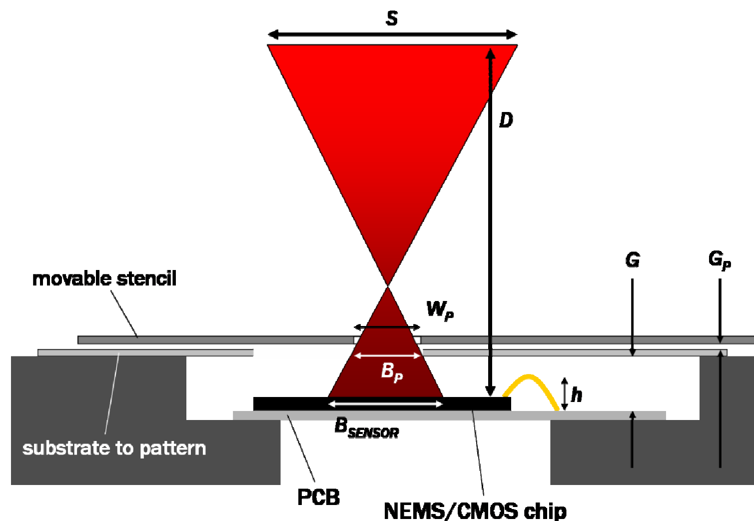

Figure 47. Schematic representation of the broadening of the flux when impacting on the sensor surface

D is the source-sample distance (≈50 cm); S the source diameter (≈1 cm); h the height of the wires (i.e. curvature, ≈1.5 mm); G the substrate-sensor gap (G≈1.5 mm, 1 mm margin respect to h); G_P the substrate-stencil gap (G_P≈10 µm, but nominally substrate and stencil are supposed to be in

contact); W_P the pattern size in the stencil (the specific pattern devoted to aligning), B_P the resulting pattern size on the substrate, and B_{SENSOR} the resulting pattern size on the surface of the sensor chip.

Let us quantify now the resulting frequency shift as a function of the deposition flux and of W_P. According to eq.IV-1, B_P is given by:

$$B_P = W_P + \frac{S\,G_P}{D} \qquad \text{(VI.25)}$$

with G_P =10 µm, $B_P = W_P$ + 200 nm. Assuming W_P in the micron range, $B_P \approx W_P$, what means that the beam is not widened when impacting after the stencil onto the substrate.

Now the lateral extension of the flux when impacting on the chip surface must be estimated. Assuming G equal to 1.5 mm:

$$B_{SENSOR} = W_P + \frac{S\,G}{D} \approx W_P + 30\mu m \approx 30\mu m \qquad \text{(VI.26)}$$

As a conclusion, the flux size on the NEMS chip surface is constant around 30 µm and is independent of W_P. This implies that the resonator receives much less flux. For a device with a given distributed mass sensitivity, this will convert into higher times before detecting anything.

To quantify this issue, a short study is carried out. First, it is assumed that the stencil is fully in front of the substrate aperture exposing it to the 'collimated' atoms beam.

The nominal flux of the deposition chamber that impacts and passes through stencil and substrate is called F_{SOURCE} (in nm/s). The resulting flux F_{SENSOR} impacting on the sensor chip surface can be expressed as:

$$F_{SENSOR} = F_{SOURCE}\frac{A_{STENCIL}}{A_{SENSOR}} \qquad \text{(VI.27)}$$

where $A_{STENCIL}$ is the area of the stencil aperture (W_P) and A_{SENSOR} the area related to B_{SENSOR}.

$A_{STENCIL}$ is approximately given for a circular hole shape by:

$$A_{STENCIL} = \pi\left(\frac{W_P}{2}\right)^2 \qquad \text{(VI.28)}$$

A_{SENSOR} , the area related to B_{SENSOR}, is approximately given for a circular shape by:

$$A_{SENSOR} = \pi\left(\frac{30\mu m}{2}\right)^2 \qquad \text{(VI.29)}$$

Now, the minimum time (t_{MIN}) of aperture of the shutter, in order to be able to detect a minimum resonance frequency variation, can be evaluated from eq.(VI.15). So:

$$\frac{S_D \, \Delta f_{MIN}}{\rho} = \Delta e_{MIN} = F_{SENSOR} \, t_{MIN} \qquad \text{(VI.30)}$$

where S_D is the distributed mass sensitivity (g.cm^{-2}.Hz^{-1}), Δf_{MIN} the minimum detectable frequency shift produced by mass loading, ρ the density of the deposition material and Δe_{MIN} the corresponding minimum detectable thickness.

Computing eq.(VI.27) and (VI.30), the minimum time to detect a mass change is expressed:

$$t_{MIN} = \frac{S_D \, \Delta f_{MIN} \, A_{SENSOR}}{\rho \, F_{SOURCE} \, A_{STENCIL}} \qquad \text{(VI.31)}$$

In Table VI - 8, t_{MIN} is reported in function of the stencil aperture size and the distributed mass sensitivity of the sensor (in the order of the ones of experiment III) with the example of silver as deposition material (ρ=10.5 g.cm^{-3}), Δf_{MIN} =10 Hz (noise level estimated from experiment III), and F_{SOURCE} =0.4 nm/s (standard value provided by the fabricant):

Stencil aperture size (µm)		1	5	10
t_{MIN} (s) for	S= 5.10^{-11}g.cm^{-2}.Hz^{-1}	1.1	0.04	0.01
	S= 10^{-10}g.cm^{-2}.Hz^{-1}	2.1	0.09	0.02

Table VI - 8. Minimum time to detect any mass-related resonance frequency variation in function of the stencil aperture size and of two distributed mass sensitivities

This table shows that the bigger is the stencil hole, the faster is the time response of the mass sensor. It may seem paradoxical but this means that the larger is the stencil hole dedicated to alignment, the better will be the alignment, i.e. the borders of substrate apertures will be easier and faster detected.

The alignment accuracy is difficult to quantify since it depends on the scanning speed, the precision of the XY actuators and on the mass sensors sensitivity (in the sense that the inflexion point of the resonance frequency evolution can be more or less precisely determined). Provided that the scanning speed is not too fast, the accuracy should be at least in the range of few microns.

Conclusion of chapter 6

In this chapter, the versatility of NEMS-based mass sensors has been illustrated through four different examples of applications.

For scientific purposes, these ultra-sensitive nanosensors open up new possibilities of exploring new physical or chemical phenomena previously unattainable with any other tools. In this thesis, the study of wetting mechanisms at very small scales (femtoliter droplets) has been made possible thanks to the use of NEMS/CMOS as nano/microbalances. Such phenomena could have not been analyzed with traditional quartz microbalances whose mass resolution is more limited.

Through the in-situ monitoring of the deposition of ultra-thin gold layers, experiment III has confirmed the very high distributed mass sensitivity of NEMS-based mass sensors.

The fact that such sensors provide an unprecedented mass sensitivity and a very high spatial resolution inherent to their small size makes them interesting devices for industrial applications as well. In this sense, applying a mass sensor like a positioning sensor has allowed developing a quasi-dynamic stencil lithography system.

Bibliographical references

1. Xia, Y.N. and G.M. Whitesides
Soft lithography
Annual Review of Materials Science, 1998. **28**: p. 153-184.

2. Thorsen, T., S.J. Maerkl, and S.R. Quake
Microfluidic large-scale integration
Science, 2002. **298**(5593): p. 580-584.

3. Delamarche, E., A. Bernard, H. Schmid, B. Michel, and H. Biebuyck
Patterned delivery of immunoglobulins to surfaces using microfluidic networks
Science, 1997. **276**(5313): p. 779-781.

4. Calvert, P.
Inkjet printing for materials and devices
Chemistry of Materials, 2001. **13**(10): p. 3299-3305.

5. Belaubre, P., M. Guirardel, G. Garcia, J.B. Pourciel, V. Leberre, A. Dagkessamanskaia, E. Trevisiol, J.M. Francois, and C. Bergaud
Fabrication of biological microarrays using microcantilevers
Applied Physics Letters, 2003. **82**(18): p. 3122-3124.

6. Piner, R.D., J. Zhu, F. Xu, S.H. Hong, and C.A. Mirkin
"Dip-pen" nanolithography
Science, 1999. **283**(5402): p. 661-663.

7. Fang, A.P., E. Dujardin, and T. Ondarcuhu
Control of droplet size in liquid nanodispensing
Nano Letters, 2006. **6**(10): p. 2368-2374.

8. Meister, A., M. Liley, J. Brugger, R. Pugin, and H. Heinzelmann
Nanodispenser for attoliter volume deposition using atomic force microscopy probes modified by focused-ion-beam milling
Applied Physics Letters, 2004. **85**(25): p. 6260-6262.

9. Picknett, R.G. and R. Bexon
Evaporation of Sessile or Pendant Drops in Still Air
Journal of Colloid and Interface Science, 1977. **61**(2): p. 336-350.

10. Dohn, S., R. Sandberg, W. Svendsen, and A. Boisen
Enhanced functionality of cantilever based mass sensors using higher modes
Applied Physics Letters, 2005. **86**(23).

11. Tamayo, J., D. Ramos, J. Mertens, and M. Calleja
Effect of the adsorbate stiffness on the resonance response of microcantilever sensors
Applied Physics Letters, 2006. **89**(22).

12. Chen, G.Y., T. Thundat, E.A. Wachter, and R.J. Warmack
Adsorption-Induced Surface Stress and Its Effects on Resonance Frequency of Microcantilevers
Journal of Applied Physics, 1995. **77**(8): p. 3618-3622.

13. Ramos, D., J. Tamayo, J. Mertens, M. Calleja, and A. Zaballos
Origin of the response of nanomechanical resonators to bacteria adsorption
Journal of Applied Physics, 2006. **100**(10).

14. Pham, N.T., G. McHale, M.I. Newton, B.J. Carroll, and S.M. Rowan
Application of the quartz crystal microbalance to the evaporation of colloidal suspension droplets
Langmuir, 2004. **20**(3): p. 841-847.

15. Joyce, M.J., P. Todaro, R. Penfold, S.N. Port, J.A.W. May, C. Barnes, and A.J. Peyton
Evaporation of sessile drops: Application of the quartz crystal microbalance
Langmuir, 2000. **16**(8): p. 4024-4033.

16. Ondarcuhu, T., L. Nicu, S. Cholet, C. Bergaud, S. Gerdes, and C. Joachim
A metallic microcantilever electric contact probe array incorporated in an atomic force microscope
Review of Scientific Instruments, 2000. **71**(5): p. 2087-2093.

17. Spletzer, M., A. Raman, A.Q. Wu, X.F. Xu, and R. Reifenberger
Ultrasensitive mass sensing using mode localization in coupled microcantilevers
Applied Physics Letters, 2006. **88**(25).

18. Sauerbrey, G.
Verwendung Von Schwingquarzen Zur Wagung Dunner Schichten Und Zur Mikrowagung
Zeitschrift Fur Physik, 1959. **155**(2): p. 206-222.

19. Miller, J.G. and D.I. Bolef
Sensitivity Enhancement by Use of Acoustic Resonators in Cw Ultrasonic Spectroscopy
Journal of Applied Physics, 1968. **39**(10): p. 4589-&.

20. Cumpson, P.J. and M.P. Seah
The Quartz Crystal Microbalance - Radial Polar Dependence of Mass Sensitivity Both on and Off the Electrodes
Measurement Science & Technology, 1990. **1**(7): p. 544-555.

21. Lu, P., H.P. Lee, C. Lu, and S.J. O'Shea
Surface stress effects on the resonance properties of cantilever sensors
Physical Review B, 2005. **72**(8).

22. Haiss, W.
Surface stress of clean and adsorbate-covered solids
Reports on Progress in Physics, 2001. **64**(5): p. 591-648.

23. Friesen, C., N. Dimitrov, R.C. Cammarata, and K. Sieradzki
Surface stress and electrocapillarity of solid electrodes
Langmuir, 2001. **17**(3): p. 807-815.

24. Racz, Z., J.L. He, S. Srinivasan, W. Zhao, A. Seabaugh, K.P. Han, P. Ruchhoeft, and J. Wolfe
Nanofabrication using nanotranslated stencil masks and lift off
Journal of Vacuum Science & Technology B, 2004. **22**(1): p. 74-76.

General Conclusion

This PhD thesis features specific results in three different directions.

First, it demonstrates through a specific application the applicability of nanostencil lithography as a novel, clean (resistless), parallel and straightforward nanopatterning technique for the full-wafer scale integration of silicon NEMS on CMOS.

With regard to this matter, this work shows that CMOS-NEMS are systems that combine two interesting features:

- they have unprecedented sensing attributes originated by the mechanical part
- they also offer the possibility to detect the sensing signal in enhanced conditions as the on-chip CMOS circuitry reduces parasitic loads and can complementarily amplify and condition the sensing signal.

Finally, several examples of applications of CMOS-NEMS as ultra-sensitive nanomechanical mass sensors have been detailed. Their results reveal the high versatility of such sensors that can be utilized both for scientific research purposes, as they allow exploring new physical, chemical or biological mechanisms at previously unexplored scales; and in industrial applications, in particular in the semiconductor industry, to control depositions of thin film or as alignment sensors in lithography systems.

In the following paragraphs, the main results are summarized.

As a first step, the mechanical and electrical behavior of electrostatically actuated nano/microresonators (cantilevers, bridges and quad-beams) embedded in a capacitive detection scheme have been analyzed. A comparative electrical study of resonators vibrating in in-plane and out-of-plane flexion has been carried out. The main issue in a capacitive detection scheme comes from parasitic stray capacitances that can drastically degrade the performance of the transduction. In this configuration, in-plane vibrating devices are much less affected than the out-of-plane ones as much higher amplitude and phase relative changes can be obtained with respect to the background signal. However in practice, in-plane vibrating resonators present reduced capacitive coupling areas what results in low absolute signal levels. Additionally, output parasitic capacitances arising from the measurement instrumentation can further reduce the available signal levels.

In this sense, the opportunity to integrate monolithically nano/micromechanical resonators on CMOS in order to detect the signal through a specific circuitry has been studied. Such

integration provides two major advantages: (i) reducing all the parasitic loads at the resonator output, and (ii) amplifying and conditioning 'on-chip' the resonance signal. Hence, a specific low-power CMOS readout circuit, whose function is to read out the capacitive current generated by a resonating nano/micromechanical device, has been designed. It is basically a transimpedance amplifier whose architecture is based on a second generation current conveyor.

Its topology and the corresponding layout have been described and the circuit behavior (intrinsic and coupled to the NEMS) has been fully simulated. According to simulation results, the detection of the resonance of a nano/microcantilever is greatly enhanced through the CMOS integration. In the case of in-plane vibrating cantilevers, this integration reduces much the signal attenuation at the resonator output, nevertheless, in the case of quad-beams resonators, the integration provides the same advantage but does not solve the issue of 'vertical' (out-of-plane) stray capacitances.

In terms of processing, combining the technology for the fabrication of nanomechanical resonators with a standard CMOS technology is challenging. In this thesis, this issue has been addressed by developing jointly with EPFL (École Polytechnique Fédérale de Lausanne) a novel post-processing technology based on nanostencil lithography. Our works demonstrate the potential of nanostencil lithography (nSL) as a parallel, straightforward and CMOS compatible patterning technique to define devices on CMOS at the 200 nm scale.

To achieve this, two critical issues have been solved: (i) the full-wafer alignment between nanostencil and CMOS substrate at 100 mm wafer scale, and (ii) the correction of pattern blurring effect to obtain an enhanced resolution. Regarding the aspect of device operation, it has been shown that post-processing CMOS wafers with nanostencil lithography does not affect the circuitry performance on the contrary to e-beam lithography, for example.

These results represent the first time that an emerging nanolithography technique has been used to pattern multiple N-MEMS devices on a whole CMOS wafer in a parallel, potentially low-cost approach. The same strategy could be extended to other examples of nanodevices, such as single electron transistors on CMOS, for which there is at present no affordable technological process that fulfill the requirements of high resolution processing at wafer scale and CMOS compatibility.

To finish with the fabrication aspects, it must be pointed out that an alternative post-processing technology of pre-fabricated CMOS wafers has also been developed. Using electron beam lithography at low electron energy, new prototypes of NEMS/CMOS have been rapidly processed with a high flexibility.

After their fabrication, fully integrated nanomechanical resonators (either cantilevers or quad-beams) have been extensively characterized electrically. Their mechanical resonance has been successfully sensed by the CMOS circuitry. Cantilevers and quad-beams have exhibited quality factors in vacuum up to 9500 and 7000 respectively. The resonance frequency could be tuned by varying the driving voltage and interesting hysteretic non-linear behaviors have been observed either in air or in vacuum

The RLC electromechanical model, which predicts the level of electrical signal produced during mechanical resonance, is found to be rather qualitative. Yet, the large number of

uncertainties regarding the resonators parameters (Young modulus, exact dimensions, underetching extension, etc...) impedes to conclude more definitively on the accuracy of the model. Taking into account all the possible errors, this model can be considered precise within one order of magnitude what is actually sufficient to define the specifications of a CMOS readout circuit. A characterization technique based on atomic force microscopy is currently being developed to determine intrinsic mechanical parameters of those resonators (such as stiffness, mode shape, etc...).

As future prospects, several improvements regarding the design of the resonator could allow obtaining better electrical responses with the same circuit topology. In the case of the quad-beams, the integration area should be placed farther from the circuit area so that it can be polarized at much higher voltages without perturbing the juxtaposed MOS transistors. In order to reduce stray capacitances, the anchors area should be minimized, for example incorporating holes in the central plate: in this way the etching time would be reduced. Concerning cantilevers, optimizing the design of the readout and driving electrodes could lead to an important reduction of the fringing field parasitic capacitance.

Finally, the versatility of NEMS-based mass sensors (all integrated on CMOS) has been illustrated through four different examples of applications.

Indeed, such ultra-sensitive nanosensors open up new possibilities of exploring new physical or chemical phenomena previously unattainable with any other tools. In the first experiment, wetting mechanisms of sessile droplets have been explored at very small scales (volumes in the femtoliter range) implementing the resonators as nano/microbalances. Such phenomena could not have been analyzed with traditional quartz microbalances whose mass resolution is more limited.

In the second experiment, a new architecture of resonator based on a double nano/microcantilever has been designed and tested: this new device allows making reliable measurements under ambient conditions by providing a direct estimation of the measurement uncertainty. Other interesting features of these double cantilevers have been described like the possibility to measure a mass loading relying on amplitude instead of frequency changes.

The fact that NEMS-based mass sensors provide an unprecedented mass sensitivity and a very high spatial resolution inherent to their small size makes of them interesting devices for industrial applications as well.

With regard to this matter, another experiment has consisted in monitoring in-situ the deposition of ultra-thin gold layers both with NEMS/CMOS and quartz-crystal microbalances. When measuring in real time the mass of these uniform deposits of thicknesses inferior to sub-monolayer, silicon nano/microresonators have exhibited a mass sensitivity better than QCM by between two and three orders of magnitude. This is very promising with regard to the possibility of replacing QCM in the semiconductor industry as a tool to monitor the deposition of thin layers.

These outstanding mass sensing attributes have led us to apply such sensors as positioning sensors according to an innovative concept. In fact, CNM and EPFL are presently developing a 'quasi-dynamic' stencil lithography system and there was initially a need to find an adequate technique to align in-situ (within the vacuum deposition chamber) the stencil with the substrate to be patterned. Nanomechanical mass sensors will accomplish this function thanks to their mass sensitivity and spatial resolution attributes.

Annex

A1. Resum en català 232
A2. Resumen en castellano 234
A3. Résumé en français 236
A4. Zusammenfassung auf Deutsch 238
A5. Glossary 239
A6. Complete diagram of the CCII CMOS circuit 240
A7. Technological processes 241
A7.1. CNM CMOS process 241
A7.2. Dummy wafers process 247
A7.3. Post-processing based on eBL 250
A7.4. Experimental results of pattern transfer of nanostencil lithography 251
A8. QSD system: schematic of the mechanical holder of the sensor 253
A9. AFM characterization of resonators: preliminary work 254
A10. List of publications 257

A1. Resum en català

Aquest treball de tesi ha estat realitzat principalment en el Centre Nacional de Microelectrònica – Institut de Microelectrònica de Barcelona (CNM-IMB), que pertany al Consell Superior d'Investigacions Científiques (CSIC) i, en part també a l' Institut de Nanotecnología de Lyon (França) que pertany al Centre Nacional d' Investigacions Científiques (CNRS, França). El doctor Francesc Pérez-Murano ha co-dirigit la tesi al CNM, i el professor Georges Brémond al INL.

El marc d'aquest treball ha estat el projecte europeu NaPa ('Emerging Nanopatterning Methods') l'objectiu del qual és desenvolupar tècniques emergents de litografia a nivell nanomètric que es puguin industrialitzar a mig termini, i les seves possibles aplicacions. En aquest sentit, els objectius principals de la tesi han estat desenvolupar (i) sistemes nanoelectromecànics (NEMS) integrats amb CMOS, i (ii) processos de fabricació basats en una tècnica avançada de nanolitografià que es diu 'nanostencil' per poder fabricar aquests sistemes monolítics.

Aquesta tesi comporta dos aspectes principals: un està relacionat amb el disseny i la operació d'un nanodispositiu mecànic i l'altre amb les tecnologies de nanofabricació. Concretament, s'ha modelat i dissenyat un ressonador nano/micromecànic de silici, després s'ha estudiat les venteges i la viabilitat d'una integració monolítica amb un circuit CMOS. De fet, els NEMS/CMOS són sistemes atractius que combinen extraordinàries propietats del sensat, proporcionades per la part mòbil mecànica, amb la possibilitat de detectar el senyal de sortida en condicions molt més favorables ja que les capacitats paràsites són reduïdes dràsticament en tractar aquesta senyal a través d'una circuitería CMOS 'on-chip' que addicionalment pot amplificar-la i acondicionar-la.

Posteriorment, aquests dispositius han estat fabricats combinant una tecnologia CMOS estandar amb mètodes emergents de nanolitografía, en particular mitjançant litografia 'nanostencil', la qual s'ha hagut de optimitzar en terminis d'aplicabilitat i resolució.

Ha estat possible després demostrar el funcionament correcte del dispositiu NEMS/CMOS fabricat: caracteritzant la resposta freqüencial de l'estructura nano/micromecànica on el senyal de sortida ha estat obtingut sota la forma d'un senyal elèctric alternatiu tractat per un circuit CMOS específic de detecció. Finalment, s'ha implementat aquest ressonador NEMS/CMOS com un sensor de massa ultra-sensible en quatre experiments diferents orientats a objectius tècnics o científics.

A continuació, es resumeix amb més detalls el treball realitzat. Com a primer pas, dos tipus de ressonadors nano/micromecanics ('cantilevers' i 'quad-beams') s'han modelat analíticament per poder estudiar la seva resposta freqüencial mecànica. Amb l'objectiu d'excitar-los i detectar-los elèctricament, s'ha optat per una tècnica capacitiva. Per tant s'ha implementat un model mixt electromecànic per poder calcular el seu comportament elèctric.

Per millorar la resposta elèctrica, s'ha dissenyat específicament un circuit CMOS de lectura i de baix consum. Funciona com amplificador de transimpedancia per convertir el corrent creat per la ressonància mecànica en un voltatge suficientment alt. A partir de simulacions, s'ha analitzat exhaustivament (i) el comportament intrínsec d'aquest circuit i (ii) quan està acoblat el ressonador mecànic.

Tot i això, la fabricació d'aquests nanodispositius integrats en CMOS constituïa un repte ja que la integració a nivell d'oblia sencera de NEMS sobre CMOS mitjançant processos no excessivament cars no havia estat demostrada encara a l' inici d'aquesta tesi. Partint d'aquesta observació, s'ha posat en marxa una col·laboració amb l'EPFL (École Polytechnique Fédérale de Lausanne, Suïssa) per desenvolupar la litografia 'nanostencil' amb l'objectiu d'integrar a escala d'oblia estructures mesoscòpiques (micro i nano) sobre circuits CMOS pre-fabricats. Després d'identificar els principals problemes inicials, s'ha pogut desenvolupar amb èxit una tecnologia de post-procés que permet integrar NEMS en CMOS mitjançant una única etapa de litografia 'nanostencil'. En paral·lel, un altre post-procés basat en una etapa de litografia per feix d'electrons ('e-beam lithography') s'ha posat a punt de manera que es poden fabricar dins de períodes breus nous prototips de nanodispositius sobre CMOS.

Aquests NEMS/CMOS han estat extensament caracteritzats elèctricament a l' aire i al buit. Les característiques principals dels espectres de ressonància, els nivells de senyal obtinguts experimentalment així com l'efecte de la tensió aplicada han estat analitzats.

Finalment, com ja ha sigut mencionat, aquests dispositius NEMS/CMOS han estat implementats com sensors de massa. Actualment, aquesta aplicació dels NEMS és una de les més explorades ja que els ressonadors nano/micromecànics ofereixen grans avantatges en termes de sensibilitat i integració de sistemes comparats amb les tradicionals microbalances de quars. Cal destacar que degut a les seves reduïdes dimensiones, no tan sols garanteixen una sensibilitat en massa molt bona sinó també una resolució espacial infinitament millor que en els dispositius de quars.

En relació a aquesta ultima aplicació, quatre experiments diferents s'han portat a terme amb els ressonadors NEMS/CMOS: (i) en col·laboració amb un grups d'investigació en química física s'ha estudiat mitjançant un ressonador nano/micromecànic aplicat com nano/microbalança l' evaporació de gotes de volums extremadament reduïts, de l'ordre del femtolitre (10^{-15}), per aprofundir els coneixements necessaris per al desenvolupament de dispositius nano/microfluídics; (ii) una nova arquitectura de ressonador, basada en una palanca doble ('doble cantilever'), s'ha dissenyat i testejat. Aquest nou dispositiu permet fer mesures de massa en condicions ambientals amb una auto-referència proporcionant la incertesa de la mesura; (iii) s'han fet proves de deposició en ultra buit de capes ultra-fines d'or (d'espessor inferior al d'una mono-capa) sobre ressonadors. D'aquesta manera, s'ha demostrat la gran sensibilitat en massa distribuïda d'aquests dispositius NEMS/CMOS, en particular al comparar la seva resposta amb la d'una microbalança de quars a la que superen per entre dos i tres ordres de magnitud en termes de sensibilitat; (iv) basant-se en els resultats de l'experiment previ de deposició d'or, s'està dissenyant un sistema 'quasi-dinàmic' de litografia nanostencil junt amb l'EPFL. Aquest sistema consisteix en efectuar deposicions successives de diferents materials a través d'un nanostencil (plantilla) desplaçat entre cada deposició: d'aquesta manera s'obtenen nanoestructures multi-materials i ultra-pures. De manera innovadora, el sensor de massa NEMS/CMOS s'ha fet servir aquí com a sensor d'alineament entre la membrana nanostencil i el substrat per litografiar.

A2. Resumen en castellano

La presente tesis ha sido realizada principalmente en el Centro Nacional de Microelectrónica – Instituto de Microelectrónica de Barcelona (CNM-IMB), que pertenece al Consejo Superior de Investigaciones Científicas (CSIC), y en parte también en el Instituto de Nanotecnología de Lyon (Francia) que pertenece al Centro Nacional de Investigaciones Científicas (CNRS, Francia). El doctor Francesc Pérez-Murano ha codirigido la tesis en el CNM, y el profesor Georges Brémond en el INL.

Este trabajo se enmarca en el proyecto europeo NaPa ('Emerging Nanopatterning Methods') cuyo objetivo es desarrollar técnicas emergentes, industrializables a medio plazo, de litografía a nivel nanométrico, y sus posibles aplicaciones. Así pues, los objetivos principales de la tesis han sido los desarrollos simultáneos (i) de sistemas nanoelectromecánicos (NEMS) integrados en CMOS, i (ii) de procesos de fabricación basados en una técnica avanzada de nanolitografía llamada 'nanostencil lithography' para poder fabricar tales sistemas monolíticos.

Esta tesis comporta dos aspectos principales: uno relacionado con el diseño y la operación de un nanodispositivo mecánico, el otro con las tecnologías de nanofabricación. En concreto, primero se ha modelado y diseñado un resonador nano/micromecánico de silicio, luego se han estudiado las ventajas y la viabilidad de una integración monolítica con circuitería CMOS. En efecto, los NEMS/CMOS son sistemas atractivos ya que combinan extraordinarias propiedades de sensado, proporcionadas por la parte móvil mecánica, con la posibilidad de detectar la señal de salida en condiciones mucho más favorables. Las capacidades parásitas son reducidas drásticamente al tratar dicha señal a través de una circuitería CMOS 'on-chip' que adicionalmente puede amplificarla y acondicionarla.

Posteriormente, estos dispositivos se han fabricado combinando una tecnología CMOS estándar con métodos emergentes de nanolitografía, en particular con la litografía 'nanostencil', que se ha tenido que optimizar en términos de resolución y aplicabilidad.

Ha sido posible luego demostrar el correcto funcionamiento del dispositivo NEMS/CMOS fabricado, caracterizando la respuesta frecuencial de la estructura nano/micromecánica cuya señal de salida está obtenida bajo la forma de una señal eléctrica alterna tratada por una circuitería CMOS específica de detección. Finalmente, se ha implementado dicho resonador NEMS/CMOS como sensor de masa ultra-sensible en cuatro experimentos distintos orientados hacia objetivos técnicos o científicos.

A continuación, se resume con más detalles el trabajo efectuado. Como primer paso, dos tipos de resonadores nano/micromecánicos ('cantilevers' y 'quad-beams') se han modelado analíticamente para poder estudiar su respuesta frecuencial mecánica. Con el objetivo de excitarlos y detectarlos eléctricamente, se ha optado por una técnica capacitiva. Por lo tanto se ha implementado un modelo mixto electromecánico para poder calcular su comportamiento eléctrico.

Para mejorar la respuesta eléctrica, se ha diseñado específicamente un circuito CMOS de lectura y de bajo consumo. Funciona como amplificador de transimpedancia para convertir la corriente creada por la resonancia mecánica en un voltaje suficientemente alto. A partir de simulaciones, se ha analizado exhaustivamente (i) el comportamiento intrínseco de este circuito y (ii) cuando está acoplado al resonador mecánico.

Sin embargo, la fabricación de tales nanodispositivos integrados en CMOS constituía un reto ya que la integración a nivel de oblea entera de NEMS sobre CMOS mediante procesos no excesivamente costosos no había sido demostrada aún al inicio de esta tesis. Debido a esto, se puso en marcha una colaboración con el EPFL (École Polytechnique Fédérale de Lausanne, Suiza) para desarrollar la litografía 'nanostencil' con el objetivo de integrar a escala de oblea estructuras mesoscópicas (micro y nano) sobre circuitos CMOS pre-fabricados. Después de identificar los principales problemas iniciales, se ha podido desarrollar con éxito una tecnología de post-proceso que permite integrar NEMS en CMOS mediante una única etapa de litografía nanostencil. En paralelo, otro post-proceso basado en una etapa de litografía por haz de electrones ('e-beam lithography') se ha puesto a punto de manera que se pueden fabricar nuevos prototipos de nanodispositivos sobre CMOS en cortos plazos de tiempo.

La caracterización eléctrica de estos NEMS/CMOS se ha llevado a cabo intensamente tanto en aire como en vacío. Han sido analizados los niveles de señal obtenidos experimentalmente, las características principales de los espectros de resonancia y el efecto de la tensión aplicada.

Finalmente, como ya ha sido mencionado, estos dispositivos NEMS/CMOS han sido implementados como sensores de masa. Actualmente, esta aplicación de los NEMS es una de las más exploradas ya que los resonadores nano/micromecánicos ofrecen grandes ventajas en términos de sensibilidad e integración de sistemas comparados con las tradicionales microbalanzas de cuarzo. Cabe destacar que debido a sus reducidas dimensiones, no tan solo garantizan una alta sensibilidad en masa sino también una resolución espacial infinitamente mayor que los dispositivos de cuarzo.

En relación a esta última aplicación, se han llevado a cabo cuatro experimentos diferentes con resonadores NEMS/CMOS: (i) en colaboración con un grupo de investigación en química física se ha estudiado mediante un resonador nano/micromecánico utilizado como nano/microbalanza la evaporación de gotas de volúmenes extremadamente reducidos, del orden del femtolitro (10^{-15}), para profundizar en los conocimientos necesarios para el desarrollo de dispositivos de nano/microfluídica; (ii) una arquitectura nueva de resonador, basada en una palanca doble ('doble cantilever'), se ha diseñado y testeado. Este dispositivo novedoso permite hacer medidas de masa en condiciones ambientales con una auto-referencia proporcionando la incertidumbre de la medida; (iii) se han hecho pruebas de deposición en alto vacío de capas ultra-finas de oro (de espesor equivalente inferior a una mono-capa) sobre resonadores. De esa manera, se ha demostrado la gran sensibilidad en masa distribuida de estos dispositivos, en particular al comparar su respuesta con la de una microbalanza de cuarzo a la que superan por entre dos y tres ordenes de magnitud a nivel de sensibilidad; (iv) basándose en los resultados del experimento previo de deposición de oro, se está diseñando, y sigue en curso, un sistema 'quasi-dinámico' de litografía nanostencil junto con el EPFL. Este sistema consiste en efectuar deposiciones sucesivas de distintos materiales a través de un nanostencil desplazado entre cada deposición: de esa manera se obtienen multi-depósitos estructurados y ultra-puros. De manera muy novedosa, el sensor de masa NEMS/CMOS se utiliza aquí como sensor de alineamiento entre la membrana nanostencil y el substrato a litografiar.

A3. Résumé en français

Cette thèse a été réalisée principalement au Centre National de Microélectronique - Institut de Microélectronique de Barcelone (CNM-IMB), qui est un organisme du Conseil Supérieur (espagnol) de la Recherche Scientifique (CSIC), et en partie à l'Institut de Nanotechnologie de Lyon, sur le site de l'INSA Lyon, qui est lui un organisme du Centre National de la Recherche Scientifique (CNRS). Le docteur Francesc Pérez-Murano a co-dirigé la thèse au CNM, et le professeur Georges Brémond à l'INL.

Le travail a été mené dans le cadre du projet de recherche européen NaPa ('Emerging Nanopatterning Methods') dont le double objectif est de développer des techniques émergentes de nanolithographie industrialisables à moyen terme, et d'en promouvoir leurs applications potentielles. Les objectifs principaux de cette thèse ont donc été les développements simultanés (i) de systèmes nanoélectromécaniques (NEMS) intégrés sur CMOS, et (ii) de procédés de fabrication basés sur une technique avancée de nanolithographie, nommée 'nanostencil' ('nanopochoir'), pour pouvoir fabriquer de tels systèmes monolithiques.

Ce travail de thèse comporte ainsi deux aspects principaux: l'un porte sur la conception et l'actionnement d'un nanodispositif mécanique, et l'autre sur les technologies de nanofabrication. Concrètement, il a tout d'abord fallu modéliser et concevoir un résonateur nano/micromécanique de silicium, puis étudier les avantages et la faisabilité d'une intégration monolithique avec circuiterie CMOS. Les NEMS/CMOS sont en effet des systèmes très attractifs qui combinent des propriétés de transduction extraordinaires, grâce à la partie mécanique mobile, avec la possibilité de détecter le signal de sortie dans des conditions beaucoup plus favorables puisque les capacités parasites sont réduites drastiquement en traitant ce signal au travers d'une circuiterie CMOS 'on-chip' qui peut en complément l'amplifier et le conditionner.

Ces dispositifs ont ensuite été fabriqués en combinant une technologie CMOS standard avec des méthodes émergentes de nanolithographie, en particulier avec la lithographie nanostencil dont il a fallu optimiser les conditions d'application et la résolution.

Il a ensuite été possible de démontrer le bon fonctionnement des dispositifs NEMS/CMOS ainsi fabriqués en caractérisant la réponse fréquentielle des structures nano/micromécaniques, le signal de sortie étant obtenu sous la forme d'un signal électrique traité par une circuiterie CMOS spécifique pour la détection. Finalement, les résonateurs NEMS/CMOS ont été implémentés comme capteurs de masse ultra-sensibles dans quatre applications distinctes orientées vers des objectifs techniques ou scientifiques.

Dans les paragraphes suivants, le contenu du travail est explicité avec plus de détails. La première étape a donc été de modéliser analytiquement trois types de résonateurs nano/micromécaniques ('cantilevers', 'ponts' et 'quad-beams') afin de pouvoir étudier leur réponse fréquentielle mécanique. Avec l'objectif de les exciter et de les détecter électriquement, un mode de détection capacitif a été sélectionné. Par conséquent, un modèle mixte électromécanique a été appliqué de manière à pouvoir calculer la réponse électrique des dispositifs mécaniques vibrants.

Afin d'améliorer cette réponse électrique, un circuit CMOS de détection de faible consommation a été conçu spécialement. Son principe de fonctionnement est celui d'un

amplificateur de transimpédance qui convertit le courant créé par la résonance mécanique en une tension de sortie suffisamment élevée. À partir de simulations, les comportement (i) intrinsèque du circuit et (ii) lorsqu'il est couplé au résonateur mécanique ont été analysés exhaustivement.

Cependant, la fabrication de tels dispositifs intégrés sur CMOS constituait au départ un défi si l'on considère que l'intégration à échelle de 'wafer' de NEMS sur CMOS selon des procédés à relativement bas coût, incluant des étapes de nanolithographie, n'avait pas encore été démontrée lorsque cette thèse a débuté. En partant de ce constat, une collaboration avec l'EPFL (École Polytechnique Fédérale de Lausanne, Suisse) a été mise en place afin de développer la lithographie 'nanostencil' avec pour objectif d'intégrer à échelle de 'wafer' entier des structures mésoscopiques (micro et nano) sur substrat CMOS pré-fabriqué. Après en avoir identifié les principaux challenges, une technologie de post-procédé permettant d'intégrer des NEMS sur CMOS au moyen d'une unique étape de lithographie nanostencil a été développée avec succès. En parallèle, un autre post-procédé, basé lui sur une étape de lithographie par jet d'électrons ('e-beam lithography'), a été mis au point de manière à pouvoir fabriquer en un temps court de nouveaux prototypes de nanodispositifs sur CMOS.

Ces NEMS/CMOS ont ensuite été caractérisés électriquement de manière exhaustive dans l'air et sous vide poussé. Les caractéristiques principales des spectres de résonance, les niveaux de signal obtenus expérimentalement ainsi que l'effet de la tension d'excitation sur la forme du spectre ont été analysés.

Finalement, ces dispositifs NEMS/CMOS ont été implémentés comme capteurs de masse. De nos jours, cette application des NEMS est l'une des plus explorées car les résonateurs nano/micromécaniques offrent d'énormes avantages comparés aux traditionnelles microbalances à quartz en termes de sensibilité et de possibilités d'intégration de système. Leur taille extrêmement réduite leur garantit non seulement une très haute sensibilité en masse mais aussi une résolution spatiale infiniment meilleure que les macro-dispositifs à quartz.

Dans ce contexte, quatre expériences différentes ont été menées à bien avec des résonateurs NEMS/CMOS: (i) en collaboration avec un groupe de recherche en chimie physique, l'évaporation de gouttes de volumes extrêmement réduits, de l'ordre du femtolitre (10^{-15} L), a été étudiée en utilisant les résonateurs comme des nano/microbalances avec l'objectif d'approfondir les connaissances des mécanismes de mouillage à ces échelles. Cet apport devrait aider à la conception de dispositifs nano/micro-fluidiques; (ii) une nouvelle architecture de résonateur basée sur une double nano/micropoutre a été conçue et testée. Ce nouveau dispositif permet de réaliser des mesures de masse fiables sous conditions ambiantes dont l'auto-référence fournit une estimation de l'incertitude de la mesure; (iii) des expériences de dépôt sous vide poussé de couches ultra-fines (d'épaisseurs équivalentes inférieures à une monocouche) d'or sur des résonateurs ont été entreprises. De cette manière, la grande sensibilité en masse distribuée de ces dispositifs a été clairement démontrée, en particulier en comparant leur réponse avec celle d'une microbalance de quartz. Il s'avère que la sensibilité des NEMS/CMOS est meilleure par entre deux et trois ordres de grandeur; (iv) en se basant sur les résultats de l'expérience précédente de dépôt d'or, un système 'quasi-dynamique' de lithographie 'stencil' a commencé à être conçu en partenariat avec l'EPFL. À terme, ce système doit pouvoir effectuer des dépôts successifs de divers matériaux à travers un nanostencil déplacé entre chaque dépôt: de cette manière des nanostructures multi-matériaux et ultra-pures seront fabricables. Selon un concept novateur, le capteur de masse NEMS/CMOS est utilisé ici comme capteur d'alignement entre la membrane nanostencil et le substrat à lithographier.

A4. Zusammenfassung auf Deutsch

Diese Doktorarbeit wurde hauptsächlich am CNM-IMB-CSIC (Centro Nacional de Microelectronica - Instituto de Microelectronica Barcelona) und am INL (Institut für Nanotechnologie von Lyon der französische Vorstand von wissenchaftliche Forschung) realisiert. Die Arbeit wurde im Rahmen des europäischen Forschungsprojekts NaPa (‚Emerging Nanopatterning Methods') durchgeführt. Dieses Projekt verfolgt die Zwecke, aufstrebende Nanolithografie Techniken zu entwickeln und Anwendungen dieser Techniken zu fördern.

Die zwei grundsätzlichen Ziele dieser Doktorarbeit waren es, nano-elektro-mechanische Systeme (NEMS) in CMOS zu integrieren(i), und ihre Fabrikationsprozesse, die auf der "Nanostencil"-Technologie basieren, zu entwickeln (ii).

Zuerst wurden drei Typen von nano-/mikromechanischen Resonatoren (‚cantilevers', ‚bridges' und ‚quad-beams') aus Silizium mechanisch modelliert und entworfen, dann wurden die Vorteile und die Machbarkeit einer monolithischen Integration mit CMOS Schaltkreisen studiert. NEMS/CMOS sind Systeme, die aussergewöhnliche Transduktionseigenschaften haben dank dem mechanisch beweglichen Teil. Das Ausgangssignal kann unter viel günstigeren Bedingungen detektiert werden, da die parasitären Kapazitäten auf Grund der CMOS Integration stark reduziert sind. Außerdem erlaubt diese Integration das Signal ‚on-chip' zu verstärken und zu verpacken. Deshalb wurde ein Low-Power CMOS-Schaltkreis für die kapazitive Detektion des Resonanz-Signals entwickelt um die elektrischen Eigenschaften weiter zu verbessern. Dieser funktioniert wie ein Transimpedanz-Verstärker, der den bei mechanischer Resonanz entstehenden geringeren Strom in eine messbare Ausgangsspannung umwandelt. Das Verhalten des Schaltkreises unter idealen Bedingungen sowie sein Verhalten mit gekoppeltem Resonator wurden simuliert und analysiert. Dafür wurde ein elektro-mechanisches Modell verwendet, um den elektrischen Verlauf der mechanischen Bauelemente zu berechnen.

Um diese Bauelemente herzustellen, wurden zwei Verfahren kombiniert: eine Standard CMOS Technologie und die Nanostencil-Lithografie, bei der die Auflösung und die Betriebsart optimiert wurden. Damit wurde die Möglichkeit der ‚full-wafer'-Integration von NEMS in CMOS nachgewiesen.

Danach, wurde das Frequenzverhalten der hergestellten NEMS/CMOS in Luft und Vakuum analysiert. Qualitäts-Faktoren bis zu 9000 wurden erreicht. Der Schaltkreis der im Rahmen dieser Doktorarbeit entwickelt wurde, erfüllte alle geforderten Spezifikationen.

Zum Schluss wurden die NEMS/CMOS Resonatoren als ultra-empfindliche Masse-Sensoren in vier verschiedenen technischen und wissenschaftlichen Anwendungen implementiert. Im Besonderen haben wir die Verdunstung von Femtoliter-Tropfen studiert. Das NEMS wurde verwendet um die Masseveränderung pro Zeit zu bestimmen. Die Ablagerung von ultra-dünnen Gold-Schichten in Vakuum wurde mit den NEMS/CMOS charakterisiert. Dies sind Anwendungsbeispiele, die die Möglichkeiten dieser viel versprechenden Bauelementen. aufzeigen.

A5. Glossary

MEMS: MicroElectroMechanical Systems

NEMS: NanoElectroMechanical Systems

CMOS: complementary metal oxide semiconductor

IC: integrated circuit

RF: radio frequency

nSL: nanostencil lithography

eBL: electron-beam lithography

NIL: Nanoimprint lithography

DUV: deep ultra-violet

A6. Complete diagram of the CCII CMOS circuit

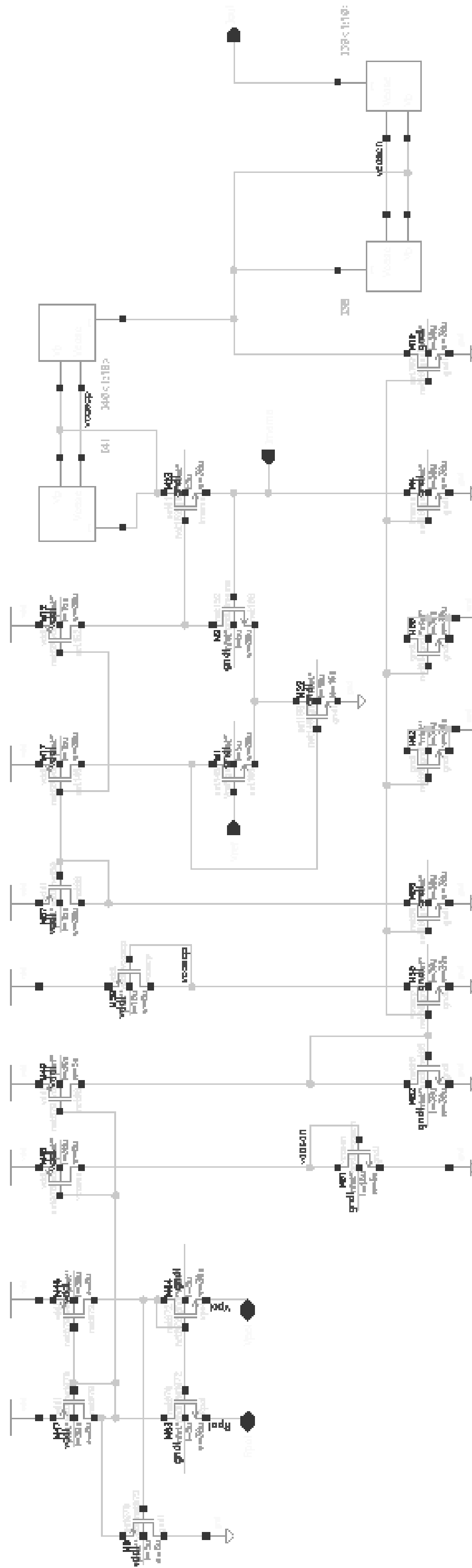

A7. Technological processes

A7.1. CNM CMOS process

In the present work, eight photolithography levels (set of reticules *CNM 264*) are required for the entire definition of the IC before its post-processing for nanomechanical structures integration. All lithographic steps are carried out with positive photoresists patterned with a NIKON stepper designed for standard UV (ultra-violet) lithography. All alignment marks are inserted inside the dicing tracks located in between chips.

N- AND P-TYPE WELLS DEFINITION (see Figure 1):

The first stage is the definition of n- and p-type wells at the surface of a p-type epitaxial Si wafer. It starts with the growth of a thin thermal 40 nm thick silicon oxide (SiO_2) on top of an ultra-clean Si surface. Then, a 120 nm thick silicon nitride (Si_3N_4) layer is deposited by Low Pressure Chemical Vapor Deposition (LPCVD) at high temperature. This Si_3N_4 layer is patterned by dry etching in a QUAD DRY TEK system using a photosensitive resist as a mask after its photolithography with dark field reticule nº1 (NTUB).

The Si_3N_4 layer acts as an implantation barrier so that n-wells can be defined by implantation of phosphorous only through its patterned apertures. After removing the resist, a thermal process leads to a growth of 400 nm of SiO_2 onto the n-wells and of a mixed nitride/oxide layer on the rest. This layer is then selectively wet etched, and the wafer surface remains covered by an oxide layer only above n-wells acting as an implantation barrier. Thus the p-wells are defined by boron implantation and the thermal oxide of the n-wells is then removed by wet etching. As a remark, this operation generates a topographical step (about 200 nm high) between p- and n-wells (located below), that creates a sufficient visual contrast allowing the posterior alignment of the second lithography reticule with the patterns of the first one.

It can be noticed also that doping implantations into silicon are generally made with a screening 20 nm thick SiO_2 layer. This implies two advantages: it avoids ion channeling into silicon bulk (what would provoke a decrease in the superficial dose) and it eliminates any risk of surface contamination possibly due to the deposition of particles arising from chamber walls after their ion bombardment due an eventual beam deflection.

Doping species are then activated by a thermal annealing (at very high temperature) under dry atmosphere. The resulting silicon oxide is immediately wet etched.

FIELD OXIDE GROWTH AND ACTIVE AREAS DEFINITION (see Figure 1):

Now both types of wells are defined, active areas (where transistors have to be integrated) must be opened into a grown field SiO_2 that ensures lateral electrical isolation between transistors. So, a 20 nm thick silicon oxide is grown and a 120 nm thick silicon nitride (Si_3N_4) layer is deposited on top by LPCVD at high temperature. The second photolithography is performed with

the so-called GASAD bright field reticule (nº2) so that it remains resist patterns only where active areas will be located.

Their definition is based on LOCOS (Localized oxidation of silicon) process. First, a nitride dry etching leaves patterns only where resist is masking, that is to say only above active areas. This nitride layer will locally act as an implantation and thermal barrier. After photoresist removal, some boron is implanted and a 1 μm thick field silicon oxide is subsequently thermally grown except where nitride patterns remain. The boron doping is used since it increases SiO_2 growth rate. The remaining oxide-nitride layer above active areas and its underneath nitride layer are wet etched. At this stage, active areas are now defined and ready for transistors integration.

A sacrificial 100 nm thick SiO_2 layer is thermally grown and a maskless boron implantation all over the wafer is performed to adjust the doping level of the future channel of the transistors: this operation adjusts precisely the threshold voltage.

POLY0 STRUCTURING, GATE OXIDE GROWTH (see Figure 1):

The *poly0* (polysilicon) layer is normally implemented as a highly doped layer to be structured as capacitor electrode for the monolithic integration of capacitors into CMOS circuits. In our case, the IC schematic does not include any capacitor but *poly0* has a fundamental importance in the process as it is implemented as structural material of the micro/nanomechanical resonators. The mechanical Q-factor of a resonating device is directly related to the internal losses and a polycrystalline structure intrinsically provides a lower Q-factor than monocristalline Si. With the aim of improving the grain structure and decreasing the surface roughness, the deposition parameters were modified with respect to a normal utilization as capacitor electrode. The thickness is adjusted to 600 nm.

So, *poly0* is deposited by LPCVD with a SiH_4 (silane) basis. Then, it was doped with $POCl_3$ by diffusion of phosphorous (n-type) at high temperature. An unwanted PSG (phosphor-silicon-glass) grows meanwhile but is removed by wet etching just after. Then, a photoresist is patterned by performing a third lithography with so-called *poly0* bright field reticule (nº3). It is hardened by a special bake so that it endures better the subsequent dry etching (APPLIED MATERIALS 5000) of polysilicon, based on chlorine chemistry. Resist is stripped and the remaining sacrificial oxide that also acted as diffusion barrier during boron doping, for threshold voltage adjustment, is removed by wet etching.

Then the gate oxide is thermally grown. Different doping levels induce different growth rates and consequently this gate oxide is 38 nm thick above active areas and 70nm thick above *poly0*. Figure 1 depicts a cross-section of the wafer at this point of the fabrication.

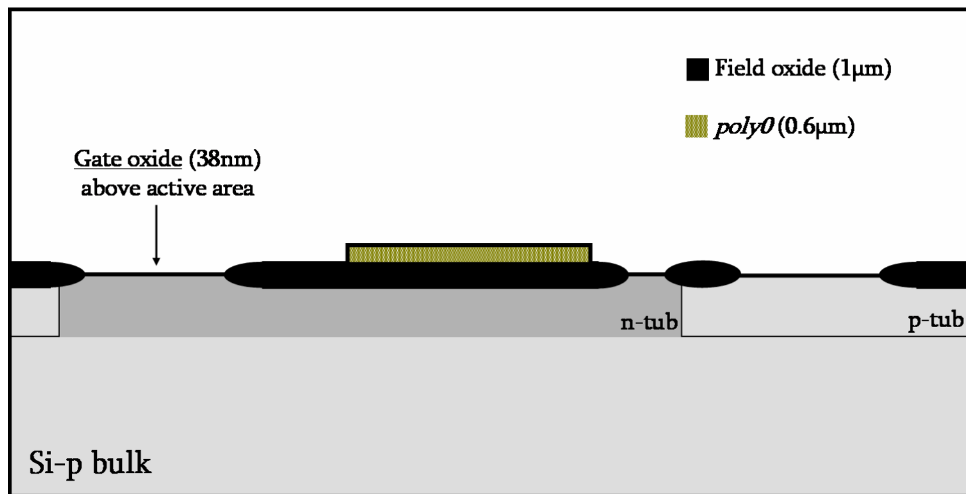

Figure 1. Part I of CMOS fabrication. Wells implantations and field oxide definition. *poly0* deposition and patterning. Gate oxide growth. NB: the topographic step between n- and p-tubs is not depicted

POLY1 STRUCTURING (see Figure 2):

Immediately after gate oxide formation, a second 480 nm thick polysilicon layer, so-called *poly1*, is deposited by LPCVD. In addition to its normal implementation as transistor gate material, it coats *poly0* within the integration areas in order to protect it during the rest of the process flow. Then a doping process based on diffusion of $POCl_3$ follows, similar to that of *poly0*.

Subsequent steps (PSG removal, photolithography with bright field *poly1* reticule [nº4], resist hardening, dry etching and resist removal) are identical to that of *poly0*.

SOURCE AND DRAIN STRUCTURING (see Figure 2):

At this stage, the transistors are almost structured: within active areas, the doping of the future channel was adjusted, a thin oxide (gate oxide) was grown and on top of it the gate was patterned. The remaining step is the functionalization of source and drain.

A photolithography with *n-plus* dark field reticule (nº5) is performed: photoresist is opened only above n-type transistors and a special bake is made in order to harden it. The subsequent implantation of P (with a dose of 4.2 10^{15} at.cm^{-2}) must define highly doped n^{++} wells so that source and drain are formed. Subsequent resist stripping requires two successive steps because of its hardness: oxygen plasma etching and wet etching.

For the definition of source and drain of p-type transistors, no photolithography is needed. This operation is realized through a maskless p-type implantation of boron (with a dose of 1 10^{15} at.cm^{-2}) that does not degrade the unmasked n-type transistors. Indeed, the level of the previous n^{++} doping is voluntarily exceeded so that this boron implantation subsequent decreases its level to reach the target value.

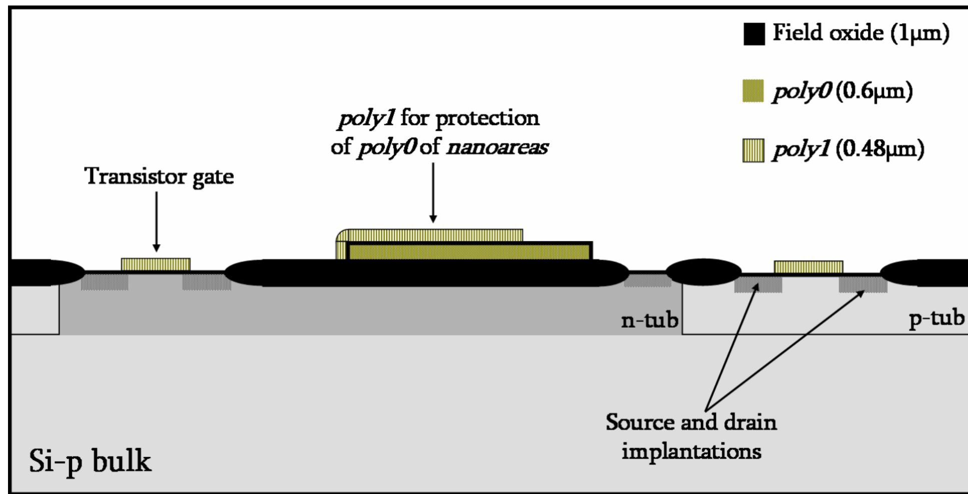

Figure 2. Part II of CMOS fabrication.
Transistor definition with gate structuring (*poly1*); source and drain doping

INTERLEVEL OXIDE STRUCTURING (see Figure 3):

CNM CMOS technology involves one single metal level and at this stage back-end operations start. The so-called *interlevel oxide* must be structured to isolate future metal interconnections from underlying layers. It is deposited by LPCVD in an AMI-DEP (APPLIED MATERIALS) with a BPTEOS (Boron-Phosphorous-Tetra-Ethyl-Ortho-Silicate) basis for a 1.3 µm target thickness. TEOS is a classical gas for the deposition of SiO_2 according to the chemical reaction:

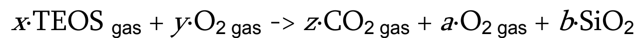

$$x \cdot TEOS_{gas} + y \cdot O_{2\,gas} \rightarrow z \cdot CO_{2\,gas} + a \cdot O_{2\,gas} + b \cdot SiO_2$$

where *x*, *y*, *z*, *a* and *b* are stoechiometric coefficients

Addition of boron and phosphorus in gaseous phase (B_2O_3 and P_2O_5) significantly improves the conformation of the deposited layer (BPSG): subsequent annealing for fluidification purposes can be made at a much lower temperature than with a standard only TEOS based oxide layer.

A photolithography with the dark field *Windows* reticule (nº6) is performed. Then with this resist masking, a dry etching is made in a DRY TEK QUAD in order to open windows accessing the underlying layers. In this way, transistors are interconnected afterwards with the metal layer. In addition, this oxide anisotropic etching must remove the gate oxide in the access windows for accessing source and drain. After this, resist is stripped and a special cleaning is made to prepare the surface to posterior metallization.

As mentioned in chapter 3, a change in the *window* reticule layout led to a drastic improvement of fabrication throughput with respect to anterior runs performed at CNM during previous research projects. In this CMOS layout, no aperture is drawn on top of the integration areas so that they remain protected by this *interlevel oxide* during posterior metal etching. Indeed,

this etch is known to be non uniform and from one point of the wafer to another removal of metal is not realized at the same speed: while in some integration areas some metal still needs to be etched, in others the process has already started to overetch and to damage the underlying non-dielectric layers, as for example the protective *poly1*.

Now, within all integration areas, apertures into *interlevel oxide* are made immediately after aperture into *passivation* layer (c.f. next paragraphs) with the same masking corresponding to the final reticule (*passivation*, nº8).

METAL LAYER STRUCTURING

The metal used in back-end for interconnections is an alloy Al / 0.5% Cu. The incorporation of Cu into Al prevents from electromigration of Al atoms during device polarization. Usually, Si-based alloys of Al are employed to prevent from the formation of spikes at aluminum/silicon interface in the contact region. Here, the doping depth in the contact region is high enough to avoid this phenomenon so that no such alloy has to be employed. A 1 µm thick layer is deposited by sputtering in a VARIAN 3180 system.

A photolithography (with bright field *Metal1* reticule, nº7) is performed with anti-reflexive photoresist. The metal layer is structured by dry etching in a DRY-TEK QUAD and the resist is removed in water. This etch is not uniform but is very selective with respect to dielectric layers, consequently as no silicon-based layer is still accessible, an eventual overetch has no consequence. This Al layer is annealed at 350ºC under forming gas for improving the quality of its interface with Si in source and drain.

PASSIVATION LAYER STRUCTURING (see Figure 3):

Let us turn to the final steps of CMOS circuit fabrication. The surface needs to be protected for packaging purposes, and has to be coated by a passivation layer that will be opened only above Al contact pads and above integration areas.

This passivation is a bi-layer of Si_3N_4 (400 nm thick) on top of SiO_2 (400 nm thick) deposited on both wafers sides by PECVD (Plasma Enhanced Chemical Vapor Deposition). This technique provides quite high deposition rates and well conformal layers but it is mainly interesting because it allows depositing at low temperature (below Al fusion point). With respect to previous CMOS runs, the thickness of Si_3N_4 was reduced thereby a too high curvature of the wafers due to silicon nitride internal stress could be avoided.

The front side of the wafer is coated with a resist and the back side is dry etched (ALCATEL GIR 160) in order to remove this bi-layer. After dielectrics removal on backside, the front side resist is stripped.

The last photolithography (CAPS dark field reticule, nº8) is performed using a non-standard resist thickness of 2 µm. This resist is hardened with a special bake so that this thermal treatment together with a bigger thickness makes it more resistant to a longer dry etching.

First, a dry etching of Si_3N_4 in DRY-TEK QUAD removes entirely the 400 nm thick layer inside the resist apertures. Once this is completed, a dry etching of oxide in DRY-TEK QUAD starts. After a penetration of 400 nm into the oxide layer, the PECVD deposited oxide is entirely removed and consequently the Al contact pads are accessed. Without being stopped, the dry etch carries on in order to remove the *interlevel oxide* on top of the integration areas while the Al contact pads are not damaged thanks to etching selectivity. A special recipe is used to obtain vertical sidewalls for a total etching depth of 1.7 μm (400 nm PECVD + 1200 nm BPSG + 130 nm thermal oxide). For easier end point detection, we included several extended test zones (400*400 μm^2) in the chip layout with such a profile: bulk silicon + gate oxide (30 nm) + *interlevel oxide* + *passivation* layers. Their big size allows monitoring the remaining SiO_2 thickness with an ellipsometric technique of large laser spot.

At this point, CMOS fabrication is completed and the wafers are now ready for post-processing with the purpose of integrating nanomechanical devices inside the integration areas:

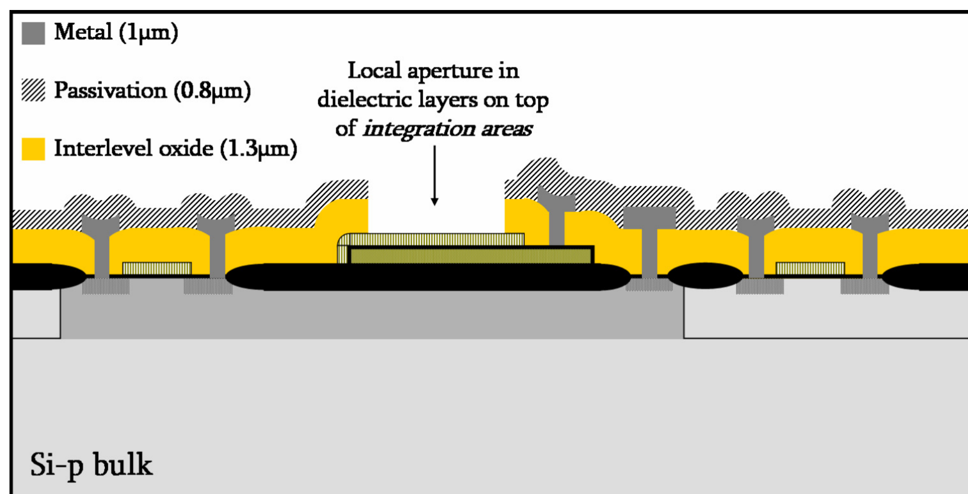

Figure 3. Final aspect at the end of the CMOS fabrication. Wafer ready for post-processing after realizing apertures in dielectric layers above the integration areas to enable posterior integration of nanodevices

A7.2. Dummy wafers process

STRUCTURE AND FABRICATION PROCESS OF DUMMIES 1: Since dummy wafers have no electrical function, they consequently have a more simple fabrication process in which all implantations and connections through *interlevel oxide* were skipped. Eight wafers were fabricated.

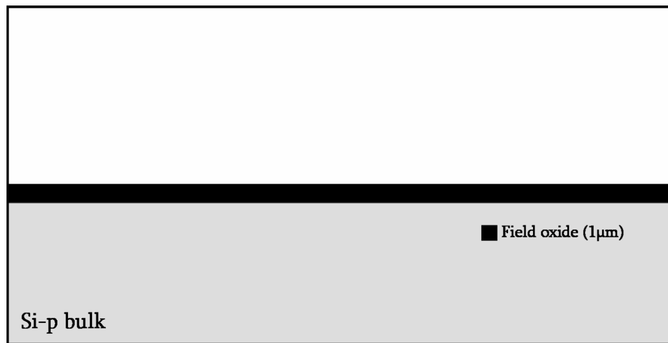

1. Growth of a 800 nm thick field SiO_2 layer

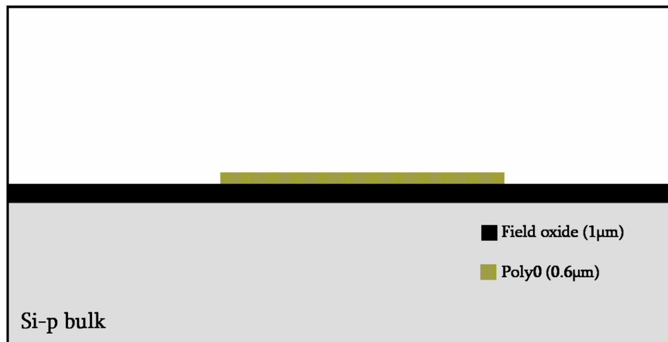

2. Deposition of a 600 nm thick *poly0* layer, $POCl_3$ doping and PSG (Phospho-silicon glass forming during doping) removal. Then, a standard UV lithography with *poly0* CMOS reticule is performed. With this resist mask, *poly0* is selectively dry etched respect to SiO_2.

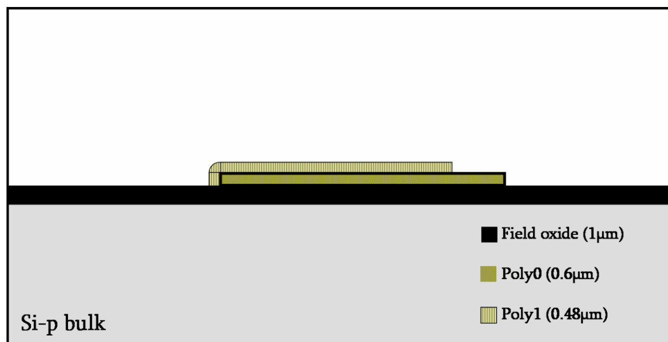

3. Pseudo "gate oxidation", deposition of a 480 nm thick *poly1* layer, $POCl_3$ doping and PSG removal. Then, a standard UV lithography with *poly1* CMOS reticule is performed. With this resist mask, *poly1* is selectively dry etched respect to SiO_2.

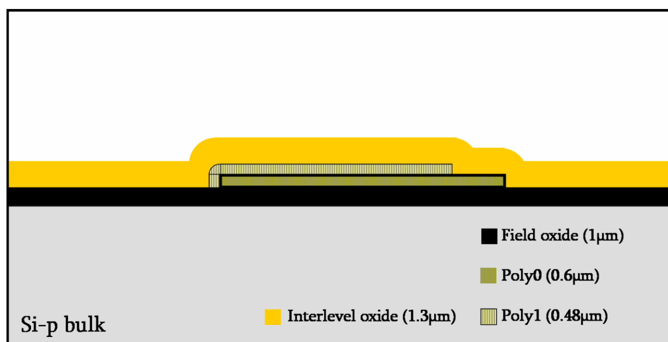

4. Deposition of a 1.1 µm thick BPSG (boro-phospho-silicon-glass, so-called *interlevel oxide*) and subsequent heat treatment for conformation to underlying topography. This layer is not patterned.

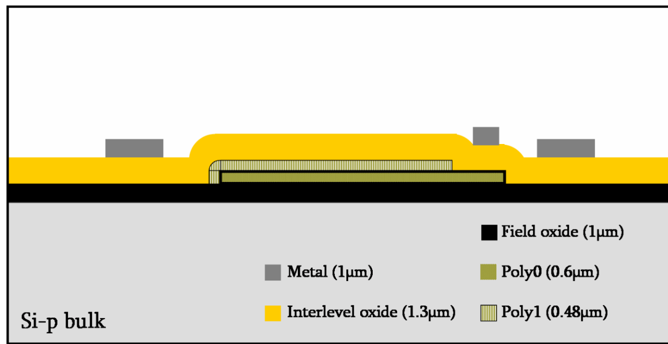

5. Metal deposition (Al, 1 µm thick) and subsequent standard UV photolithography and dry etching. As the *interlevel oxide* was not structured, the Al layer is not interconnected to underlying layers but this is not the purpose of dummies 1.

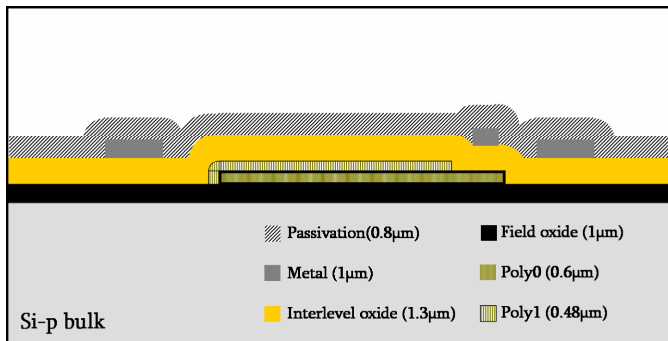

6. Deposition of a 0.8 µm thick passivation layer by PECVD (plasma enhanced chemical vapor deposition) technique.

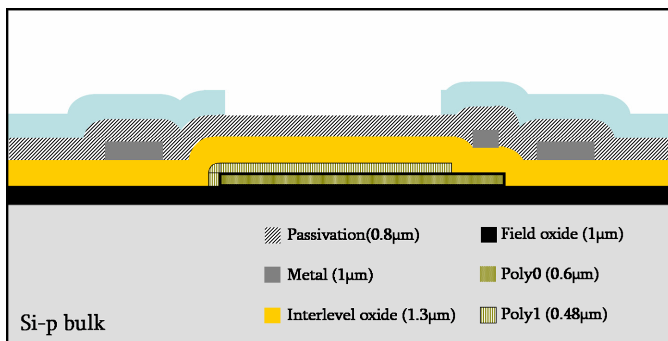

7. Standard UV lithography with CMOS *passivation layer* reticule. Given that the following step, and the first issue to be tested, is the dry etching in one single step of both *interlevel oxide* and *passivation* layers, the resist thickness is doubled.

STRUCTURE AND FABRICATION PROCESS OF DUMMIES 2:

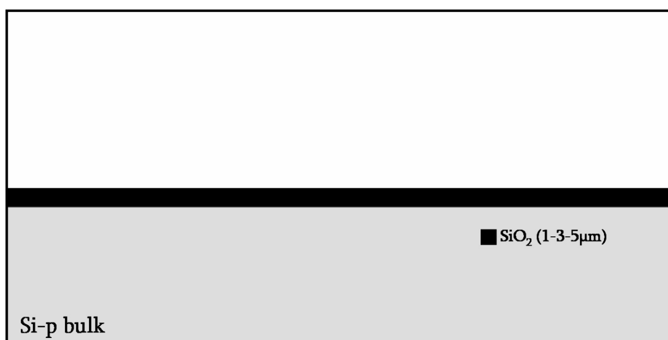

1. Deposition of a SiO_2 layer of variable thickness (1-3-5µm)

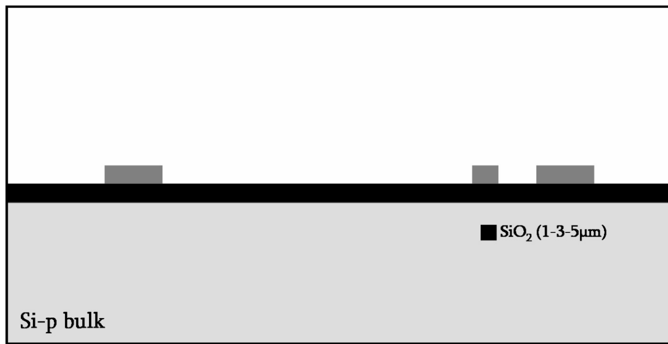

2. Deposition of a metal layer (Al, 500 nm thick) and photolithography with *metal* CMOS reticule. Al dry etching and resist removal.

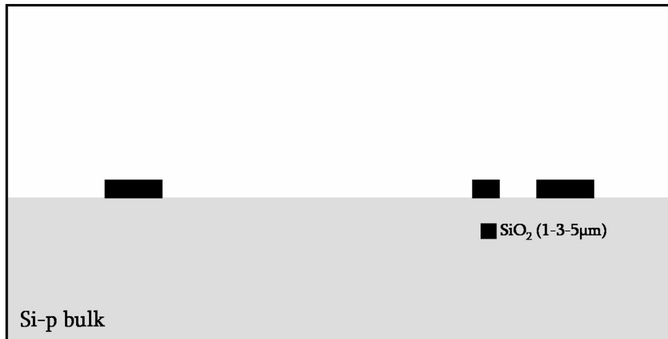

3. SiO_2 dry etching with Al as etch mask, then Al removal.

A7.3. Post-processing based on eBL

PMMA DEPOSITION, E-BEAM EXPOSURE OF PMMA AND PMMA DEVELOPMENT

Same procedure as for discrete devices made by eBL (c.f. chapter 2), except the exposure made at 3 kV (dose ~30 $\mu C/cm^2$). This lower voltage should not result in a degradation of the performance of the CMOS circuits

METALLIZATION

idem as for discrete devices made by eBL (c.f. chapter 2), but with a 32 nm thick Al layer

LIFT-OFF

like for discrete devices made by eBL (c.f. chapter 2), but without ultra-sounds to avoid that the metal strips in high-topography zones

PATTERN TRANSFER BY RIE

- RIE of the thin SiO_2 layer (70 nm thick) with Al mask structured by EBL and lift-off:

  System: GIR 160 Alcatel (recipe PGIOXGUI)
  t: 1min 30s
  CHF_3: 50 sccm
  Pressure: 5.10^{-2} mbar
  Power: 500 W
  Nominal etching speed: 100 nm/min at RT

- RIE of the structural polySi layer (~600 nm thick) with the same Al mask

  Same procedure as for discrete devices (c.f. chapter 2)

  System: Alcatel A601-E (recipe *Nano1*)
  t: 14 s + 14 s + 7s (3 discontinued steps, one entire gas cycle corresponds to 3.5 s)
  C_4F_8: 100 sccm (1s)
  SF_6: 150 sccm (2.5s)
  Pressure: 1.4 – $2.8.10^{-2}$ mbar
  ICP Power: 1500 W
  Plate power: 15 W
  Nominal etching speed: 1300 nm/min at 20ºC

RESONATORS RELEASE

The same process is used as for devices defined by nSL (see chapter 4)

A7.4. Experimental results of pattern transfer of nanostencil lithography

ANNEX ON BLURRING DATA

Dummy wafer 1-2

Chip	ΔW(nm) for cantilevers	ΔW(nm) for paddles
2	100	225
8	100	245
12	110	230
16	110	245

CMOS wafer nº11

Chip	ΔW(nm) for cantilevers	ΔW(nm) for paddles
2	140	190
23	250	250

ΔW is the blurring extension and is given by eq.(IV.1). Experimental measurements based on SEM images are reported in those tables for dummies and true CMOS wafers. Unstabilized full-wafer stencils were used, this is why ΔW is bigger for paddles since its design makes the membrane more sensible to stress during material loading.

ANNEX ON PATTERN TRANSFER DATA

In this section, pattern transfer data based on SEM images measurements are reported. Clogging effect (reduction of stencil aperture size after deposition), membrane stress with Al loading (high ΔW in the case of paddles), displacement effect (chips located in the border e.g. nº2, 8 or 12 exhibit a smaller pattern than the stencil aperture size) are well visible. When membrane is stable (in the present case membranes for cantilevers, in the future every corrugated membrane), an average deviation less than 10% is achieved.

Data measured on dummy wafers 1 and 2

(1) Data measured on cantilever patterns

Chip	Aperture size in stencil (nm)	Aperture size in stencil (nm) after evaporation	Deposited main pattern dimension (nm)	Δ stencil-deposited pattern (nm) *Left: initial; Right: final*		Deviation (%) *Left: initial stencil size Right: final stencil size*	
2	304	223	248	-56	+25	-18%	+11%
	335	341	335	0	-6	Idem	-2%
8	434	403	409	-25	+6	-6%	-1%
	546	564	509	-37	-55	-7%	-10%
12	391	335	385	-6	+50	-1.5%	+15%
	478	490	465	-13	-25	-3%	-5%
16	471	422	490	19	+68	+4%	+16%
	571	546	602	31	+56	+5%	+10%

(2) Data measured on paddle patterns

Chip	Aperture size in stencil (nm)	Aperture size in stencil (nm) after evaporation	Deposited main pattern dimension (nm)	Δ stencil-deposited pattern (nm) *Left: initial; Right: final*		Deviation (%) *Left: initial stencil size Right: final stencil size*	
2	459	682	471	+12	-211	+2.6%	-31%
8	515	757	633	118	-124	+23%	-16%
12	521	782	639	118	-143	+23%	-18%
16	552	602	633	81	+31	+18%	+5%

Data measured on CMOS wafer nº11

(1) Data measured on cantilever patterns

Chip	Aperture size in stencil (nm)	Aperture size in stencil (nm) after evaporation	Deposited main pattern dimension (nm)	Δ stencil-deposited pattern (nm) *Left: initial; Right: final*		Deviation (%) *Left: initial stencil size Right: final stencil size*	
2	310	223	236	-74	+13	-24%	+6%
	397	304	329	-68	+25	-17%	+8%
23	275	285	291	+16	+6	+6%	+2%
	409	366	378	-31	+12	+5%	-8%

(2) Data measured on paddle patterns

Chip	Aperture size in stencil (nm)	Aperture size in stencil (nm) after evaporation	Deposited main pattern dimension (nm)	Δ stencil-deposited pattern (nm) *Left: initial; Right: final*		Deviation (%) *Left: initial stencil size Right: final stencil size*	
2	370	403	397	+27	-6	+7%	-1%
23	333	385	378	+45	-7	+13%	-2%

A8. QSD system: schematic of the mechanical holder of the sensor

Figure 4. 3D representation of the mechanical holder (in grey) with the fixed PCB (large green plate) containing the CMOS/NEMS sensor (small green plate). The clips located on the border are for clamping the substrate

Figure 5. Mechanical schematic of the mechanical holder of the PCB+CMOS/NEMS chip

A9. AFM characterization of resonators: preliminary work

The atomic force microscope (AFM) potentially constitutes an alternative tool to measure the mechanical response of a nanomechanical resonator [1, 2], in particular the detect its oscillations [1, 3, 4]. In the framework of this thesis, some preliminary work has been undertaken at INL (at INSA Lyon) to explore this method. Several possible applications have been identified:

(1) applying a force with a relatively stiff tip and measuring its deflection should help in determining the spring constant of the resonant device

(2) exciting electrostatically with a DC voltage and measuring the deflection of an appropriate low-stiffness AFM cantilever applied on the resonator should allow determining the static bending of the mechanical structure and thereby obtaining information on its electromechanical behavior

(3) exciting electrostatically with an AC voltage, the frequency spectrum of the resonator could be measured and the vibration mode shapes could be 'imaged'. For this purpose, a new technique needs to be developed. As a basis, we have inspired from the lock-in detection technique of A. San Paulo et al. [3, 4]

(4) another interesting experiment would consist in approaching an AFM tip from a vibrating nanomechanical resonator and analyzing the perturbation of its frequency response generated by the interaction between both elements. For this purpose, the frequency response of a CMOS integrated nanomechanical resonator, like the ones presented in this thesis, could be electrically measured to observe any effect on the response when approaching the tip. This experiment can lead to a force calibration of the nanomechanical sensor.

Experiments of static bending of quad-beams have been performed. An excitation voltage was applied on the substrate to drive the resonator but the high voltage that was required likely perturbed the AFM cantilever. Either in contact or in tapping mode, the signal of the piezo-tube was measured while the excitation voltage was progressively increased: very large deflections of the central plate seemed to be produced but paradoxically the central plate apparently tended to get farther from the substrate (see Figure 6) what is not coherent since the plate should be electrostatically attracted. This apparent upwards bending is maybe caused by a bending downwards of the AFM cantilever due to the electrostatic attraction of the substrate: consequently the piezo-tube probably tries to compensate by retracting.

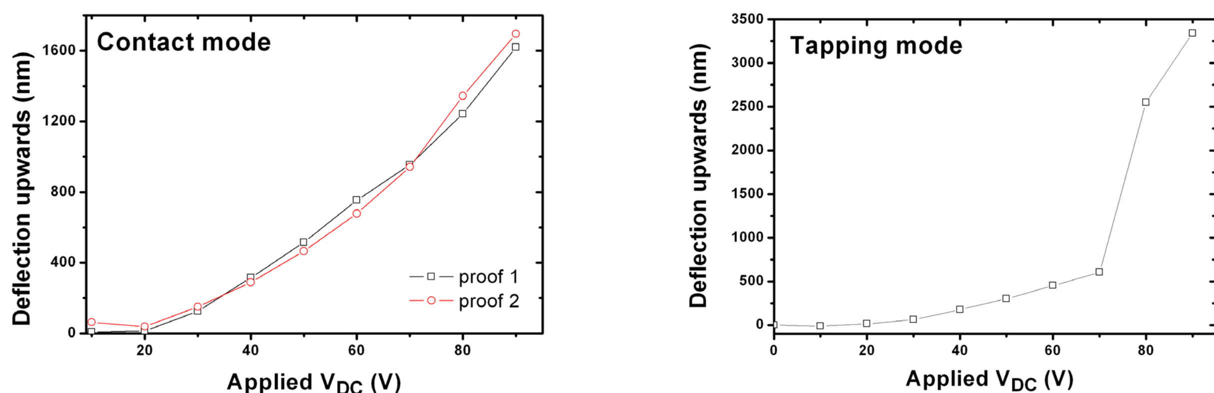

Figure 6. Measurements of the static deflection of the QB central plate by operating the AFM either in contact (left) or in tapping (right) modes [measurement of the signal of the AFM piezo-tube]

This issue should be circumvented working with undoped non-conductive AFM probes.

Dynamic electromechanical characterization has been carried out measuring the signal of the position sensitive photodiode of the AFM set-up but this signal was very noisy and difficult to stabilize. Furthermore, a very pronounced parasitic peak observed at 2.8 MHz, even when the tip was not in contact with the resonator, perturbed the measurement (this peak is attributed to the electronics of the AFM, DIMENSION 3100, VEECO INC.).

Then, the lock-in detection technique presented in [3, 4] has been adapted to the quad-beam device. In this method, the tip is placed in contact with the center of the QB plate: a sinusoidal amplitude-modulated high frequency signal (in the range of the resonance frequency of the QB), with a modulation frequency inferior to the resonance frequency of the AFM cantilever, is applied to the substrate to drive the resonator. The high frequency oscillation amplitude is measured using the modulation signal as a reference for the lock-in amplification of the photodiode signal of cantilever deflection.

The choice of an adequate frequency of modulation is important to ensure that the oscillation amplitude is only related to a mechanical resonance and not to any thermal expansion effect [3, 4]. For this purpose, we set the high frequency component at the expected resonance frequency while the vibration amplitude was measured with this technique as a function of the modulation frequency:

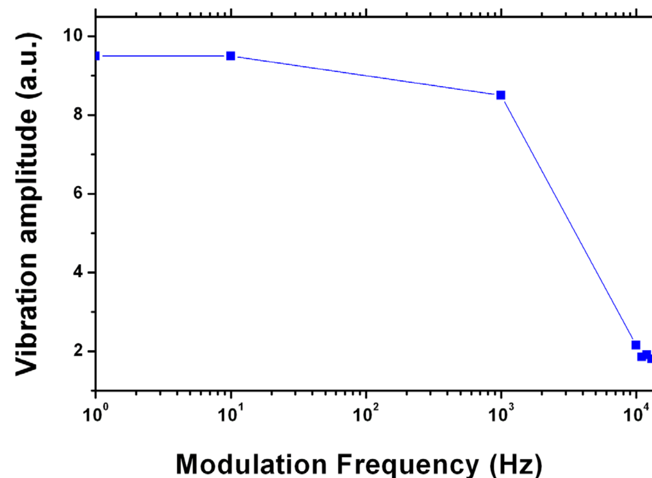

Figure 7. Vibration amplitude measured at the expected resonance frequency (2.5 MHz) as a function of the modulation frequency

This graph is consistent with what is observed in the papers [3, 4]: the system vibrates more for low modulation frequencies. Attributing this to a thermal effect, the modulation frequency is set at 5 kHz to ensure that the mechanical behavior is the dominant mechanism of vibration. Then, the frequency spectrum is measured for $V_{IN\,DC}$ = 35 V and $V_{IN\,AC}$ = 5 V peak-peak. The result is plotted in Figure 8. A peak is found around 2.35 MHz what is consistent with the expected range of resonance. However this experiment needs to be repeated and the device should also be measured with an alternative technique to corroborate the peak detected by AFM.

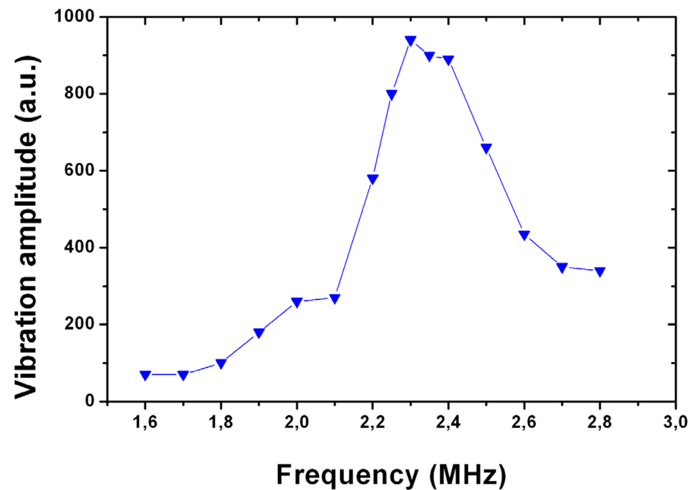

Figure 8. Frequency spectrum of a quad-beam measured by the lock-in detection technique with the AFM

Future experiments are scheduled for September 2007 with a double aim: (i) repeating the implementation of the lock-in detection technique to measure frequency spectra and (ii) analyzing the perturbation generated by the AFM tip on an oscillating CMOS nanomechanical resonator whose response is constantly detected electrically through the CMOS circuitry.

BIBLIOGRAPHICAL REFERENCES

1. Abadal, G., Z.J. Davis, X. Borrise, O. Hansen, A. Boisen, N. Barniol, F. Perez-Murano, and F. Serra
Atomic force microscope characterization of a resonating nanocantilever
Ultramicroscopy, 2003. **97**(1-4): p. 127-133.

2. Ollier, E., L. Duraffourg, M. Delaye, H. Grange, S. Deneuville, J. Bernos, R. Dianoux, F. Marchi, D. Renaud, T. Baron, P. Andreucci, and P. Robert
NEMS Devices for Accelerometers Compatible with Thin SOI Technology
in the proceedings of the *2nd IEEE International Conference on Nano/Micro Engineered and Molecular Systems*. 2007. Bangkok, Thailand.

3. San Paulo, A., X. Liu, and J. Bokor
Atomic Force Microscopy characterization of electromechanical properties of RF acoustic bulk wave resonators
in the proceedings of the *IEEE MEMS*. 2004.

4. San Paulo, A. and J. Bokor
Scanning acoustic force microscopy characterization of thermal expansion effects on the electromechanical properties of film bulk acoustic resonators
Applied Physics Letters, 2005. **86**(8).

A10. List of publications

ARTICLES ALREADY PUBLISHED

1. J. Arcamone, G. Rius, G. Abadal, J. Teva, N. Barniol, and F. Pérez-Murano

   Mechanical resonator for distributed mass sensing and capacitive detection

   Microelectronic Engineering 83, pp.1216-1220 (2006)

2. J. Arcamone, A. Sánchez-Amores, J. Montserrat, M.A.F. van den Boogaart, J. Brugger, and F. Pérez-Murano

   Dry etching for the correction of gap-induced blurring and improved pattern resolution in nanostencil lithography

   Journal of Micro/Nanolithography, MEMS and MOEMS 6 (1), 013005 (2007)

3. J. Arcamone, B. Misischi, F. Serra-Graells, M.A.F. van den Boogaart, J. Brugger, F. Torres, G. Abadal, N. Barniol, and F. Pérez-Murano

   A compact and low-power CMOS circuit for fully integrated NEMS resonators

   IEEE Transactions on Circuits and Systems II, 54 (5) pp 377-381 (2007)

ARTICLES ALREADY SUBMITTED

4. J. Arcamone, B. Misischi, F. Serra-Graells, M.A.F. van den Boogaart, J. Brugger, F. Torres, G. Abadal, N. Barniol, and F. Pérez-Murano

   A compact CMOS current conveyor for integrated NEMS resonators

   SPRINGER Journal of Analog Integrated Circuits and Signal Processing

ARTICLES IN PREPARATION

5. J. Arcamone, M.A.F. van den Boogaart, A. Sanchez-Amores, J. Montserrat, J. Fraxedas, F. Torres, G. Abadal, N. Barniol, J. Brugger and F. Pérez-Murano

   Fabrication of attogram sensitivity micro-nanomechanical mass sensors based on a full wafer integration on CMOS by nanostencil lithography

   to be submitted to the IEEE Journal of Microelectromechanical systems

6. J. Arcamone, G. Rius, J. Llobet, X. Borrise and F. Pérez-Murano

   Mass measurements based on nanomechanical devices: differential measurements

   to be submitted to the IEEE Transactions on Nanotechnology

7. J. Arcamone, E. Dujardin, G. Rius, F. Pérez-Murano and T. Ondarçuhu
Monitoring the evaporation of femtoliter sessile droplets with CMOS integrated nanomechanical mass sensors
to be submitted to the ACS Journal of Physical Chemistry B

Contributions at national and international scientific conferences

1. J. Arcamone, G. Rius, X. Borrisé and F. Pérez-Murano
Combination of e-beam and UV lithography for the prototyping of nano-mechanical devices
poster at the Nanospain conference, March 2005, Barcelona (Spain)

2. J. Arcamone, G. Rius, G. Abadal, J. Teva, N. Barniol and F. Pérez-Murano
Micro/nanomechanical resonators for distributed mass sensing with capacitive detection
poster at the MNE (Micro/NanoEngineering) conference, September 2005, Vienna (Austria)

3. J. Arcamone, A. Sánchez-Amores, L. Doeswijk, M.A.F. van den Boogaart, J. Brugger and F. Pérez-Murano
Pattern recovery by dry etching of gap-induced blurring in nanostencil lithography
poster at the MNE (Micro/NanoEngineering) conference, September 2005, Vienna (Austria)

4. F. Torres, J. Arcamone, J. Teva, J.LL. Lopez, A. Uranga, G. Abadal, N. Barniol and F. Perez-Murano
Beam shape resonator made from EBL and RIE techniques
poster at the Nanospain conference, March 2006, Pamplona (Spain)

5. J. Arcamone, G. Rius, and F. Pérez-Murano
Micro/nanomechanical resonators for distributed mass sensing with capacitive detection
poster at the International Workshop on Nanomechanical Sensors, May 2006, Copenhagen (DK)

6. J. Arcamone, M.A.F. van den Boogaart, F. Serra-Graells, S. Hansen, J. Brugger, F. Torres, G. Abadal, N. Barniol, and F. Pérez-Murano
Full-wafer integration of NEMS on CMOS by nanostencil lithography
oral presentation at the IEEE IEDM 2006 (International Electron Devices Meeting), December 2006, San Francisco (USA)

7. J. Arcamone, T. Ondarçuhu, E. Dujardin, G. Rius, and F. Pérez-Murano
Characterization of femtoliter droplets with nanomechanical mass sensors
oral presentation at the International Workshop on Nanomechanical Sensors, May 2007, Montreal (Canada)

8. J. Arcamone, M.A.F. van den Boogaart, F. Serra-Graells, J. Fraxedas, J. Brugger, F. Torres, G. Abadal, N. Barniol, and F. Pérez-Murano

Nanomechanical mass sensors based on a full-wafer integration of NEMS on CMOS by nanostencil lithography

poster at the International Workshop on Nanomechanical Sensors, May 2007, Montreal (Canada)

9. F. Torres, G. Abadal, J. Arcamone, J. Teva, J. Verd, A. Uranga, J.Ll López, X. Borrisé, F. Pérez-Murano and N. Barniol

Coupling resonant micro and nanocantilevers to improve mass responsivity by detectability product

oral presentation at the IEEE Transducers conference, June 2007, Lyon (France)

10. J. Verd, A. Uranga, J. Teva, G. Abadal, F. Torres, J. Arcamone, J.Ll López, F. Pérez-Murano, J. Fraxedas, J. Esteve and N. Barniol

Monolithic 0.35 µm CMOS cantilever for mass sensing in the attogram range with self-excitation

oral presentation at the IEEE Transducers conference, June 2007, Lyon (France)

11. J. Arcamone, T. Ondarçuhu, E. Dujardin, G. Rius, and F. Pérez-Murano

Monitoring the evaporation of femtoliter droplets with CMOS integrated nanomechanical mass sensors

oral presentation at the IEEE Sensors conference to be held in October 2007, Atlanta (USA)